MAGYAR ÁLLAMI
EÖTVÖS LORÁND
GEOFIZIKAI INTÉZET

GEOFIZIKAI
KÖZLEMÉNYEK

ВЕНГЕРСКИЙ
ГЕОФИЗИЧЕСКИЙ
ИНСТИТУТ
ИМ Л. ЭТВЕША

ГЕОФИЗИЧЕСКИЙ
БЮЛЛЕТЕНЬ

GEOPHYSICAL

TRANSACTIONS

EÖTVÖS LORÁND GEOPHYSICAL INSTITUTE OF HUNGARY

CONTENTS

VOL. 45. NO. 3. September 2008. (ISSN 0016-7177)

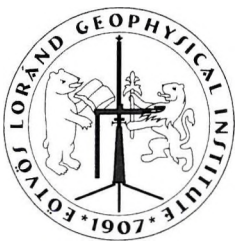

TARTALOMJEGYZÉK

GEOPHYSICAL TRANSACTIONS 2008
Vol. 45. No. 3. pp. 105– 121

Determining the objective function for geophysical joint inversion

Dezső DRAHOS*

A serious problem in joint inversion is that of selecting those particular weight factors which control the correct contribution of each individual data set to the joint objective function. These weight factors are necessary input parameters of joint inversion but generally they are unknown. A method is proposed in which there is no need to know these weight factors. The maximum likelihood principle is applied so that optimization is done not only by the model parameters but also by the standard deviations of the data. The application is demonstrated by joint inversion of various simulated erroneous data sets. Linear toy examples of two data sets were studied for various common and uncommon model parameters. Experience has shown that with increasing number of data the estimates of the model parameters and the standard deviations of the data approximate their true values. Several simulated geophysical joint inversion problems were studied: gravity and magnetic, log evaluation, and refraction seismic. These examples show the applicability of the method.

Keywords: joint inversion, gravity, magnetics, log evaluation, refraction seismics

1. Introduction

Inversion of various data sets can be done independently (sequentially) for each type of measurement or it can be done jointly. Joint inversion is widely used because it produces mutually consistent estimates of the various unknown parameters [JULIÀ et al. 2000]. The purpose of joint inversion is that one objective function to be optimized is produced from the individual objective functions representing the various data sets. The usual strategy is to add the objective functions that create the joint objective function, but the magnitudes and the dimensions of the component objective functions are different. To overcome this difficulty, the difference between the observed data and the computed theoretical value can be normalized by the measured one. DOBRÓKA et al. [1991] and DE

* Eötvös Loránd University, Faculty of Science, Institute of Geography and Earth Sciences, Department of Geophysics, 1117 Budapest, Pázmány P. sétány 1/C Hungary.

Manuscript received: 24 February, 2008

NARDIS et al. [2005] utilized this strategy. A further problem is that the quality of the different types of measurement may differ, therefore the component objective functions should be multiplied by weight factors thereby giving them the correct contribution for determining the model parameters. JULIÀ et al. [2000] introduced the 'influence parameter' p, which is responsible for the correct contribution between the seismic receiver function and the dispersion data sets. A similar method was applied in MOTA, MONTEIRO DOS SANTOS [2006], where resistivity and seismic velocity data were inverted jointly with weights α and $1-\alpha$ for the resistivity data and velocity data respectively. The parameters p and α are determined by repeated inversion experiments. There is no general rule for selecting these weight factors even though the results depend on them. TREITEL and LINES [1999] mentioned it as a big unsolved problem of joint inversion. A method is proposed here in which there are no input weight factors and the component functions provide the correct contribution to the joint objective function.

2. Method

Let us consider two different types of geophysical measurement. The sets of data and the corresponding sets of theoretical functions relating to the model are denoted by the vectors $\mathbf{d}_1$, $\mathbf{G}_1(\mathbf{m})$ and $\mathbf{d}_2$, $\mathbf{G}_2(\mathbf{m})$ respectively. They are referenced herein as task 1 and task 2. The dimensions of the vectors are n_1 and n_2. The unknown model parameters to be determined are the components of the vector $\mathbf{m}$, the dimension of which is n_m. The following scheme describes the connection between the measured and the theoretical quantities for task 1 and task 2:

$$\mathbf{d}_1 = \mathbf{G}_1(\mathbf{m}) + \mathbf{e}_1 \tag{1}$$

and

$$\mathbf{d}_2 = \mathbf{G}_2(\mathbf{m}) + \mathbf{e}_2 \tag{2}$$

In the above equations, vectors $\mathbf{e}_1$ and $\mathbf{e}_2$ represent the noise, these vectors are independent random numbers. It is assumed that they show normal distribution with zero expected values. The standard deviation for the $\mathbf{e}_1$'s is σ_1 and for the $\mathbf{e}_2$'s it is σ_2. It is important to note that these two

standard deviations are also unknown. The usual form of the joint objective function of the L_2 norm is

$$\lambda = w_1 \sum_{i=1}^{n_1} (d_{1,i} - G_{1,i}(\mathbf{m}))^2 + w_2 \sum_{j=1}^{n_2} (d_{2,j} - G_{2,j}(\mathbf{m}))^2, \tag{3}$$

where w_1 and w_2 are the weight factors. The minimum of λ determines the model parameter estimates which depend also on the weight factors, but these weight factors are generally unknown. If the maximum likelihood principle [KENDALL, STUART 1967] is applied separately to task 1 and task 2, the likelihood functions l_1 and l_2 should be maximized with respect to $\mathbf{m}$. The mathematical form of the likelihood functions is:

$$l_1 = f_1(d_{1,1}, \mathbf{m}) f_1(d_{1,2}, \mathbf{m}) \ldots f_1(d_{1,n_1}, \mathbf{m}) \tag{4}$$

where

$$f_1(d_{1,i}, \mathbf{m}) = \frac{1}{\sqrt{2\pi}\,\sigma_1} \exp\left(-\frac{1}{2\sigma_1^2} (d_{1,i} - G_{1,i}(\mathbf{m}))^2 \right), \tag{5}$$

[MENKE 1989] and similarly:

$$l_2 = f_2(d_{2,1}, \mathbf{m}) f_2(d_{2,2}, \mathbf{m}) \ldots f_2(d_{2,n_2}, \mathbf{m}) \tag{6}$$

where

$$f_2(d_{2,j}, \mathbf{m}) = \frac{1}{\sqrt{2\pi}\,\sigma_2} \exp\left(-\frac{1}{2\sigma_2^2} (d_{2,j} - G_{2,j}(\mathbf{m}))^2 \right). \tag{7}$$

By maximizing l_1 and l_2, two independent estimates of $\mathbf{m}_1$ and $\mathbf{m}_2$ are determined respectively. The aim of joint inversion is that one common estimate of $\mathbf{m}$ is to be determined which corresponds to both $\mathbf{d}_1$ and $\mathbf{d}_2$ data. Therefore the product $l = l_1 l_2$ should be maximized. The complete form of l is:

$$l = \frac{1}{(\sqrt{2\pi})^{n_1+n_2} \sigma_1^{n_1} \sigma_2^{n_2}} \exp\left\{ -\frac{1}{2\sigma_1^2} \sum_{i=1}^{n_1} (d_{1,i} - G_{1,i}(\mathbf{m}))^2 - \frac{1}{2\sigma_2^2} \sum_{j=1}^{n_2} (d_{2,j} - G_{2,j}(\mathbf{m}))^2 \right\} \tag{8}$$

Function l depends on the measured data, the model parameters, and the standard deviations. This is the joint objective function for task 1 and task 2. By maximizing l, the estimates of the model parameters are determined. The usual way to solve the problem is to minimize the negative logarithm λ of function l:

$$\lambda = -\ln(l) \tag{9}$$

that is

$$\lambda = \frac{n_1 + n_2}{2}\ln(2\pi) + n_1 \ln\sigma_1 + n_2 \ln\sigma_2 + \frac{1}{2\sigma_1^2}\sum_{i=1}^{n_1}(d_{1,i} - G_{1,i}(\mathbf{m}))^2 + \\ + \frac{1}{2\sigma_2^2}\sum_{j=1}^{n_2}(d_{2,j} - G_{2,j}(\mathbf{m}))^2 \quad . \tag{10}$$

If the standard deviations σ_1 and σ_2 are known, the minimization relates only to the rightmost two members of eq. 10, which is equivalent to the minimization of λ in eq. 3. On comparing eqs. 3 and 10 it can be seen that the true values of the weights are:

$$w_1 = \frac{1}{2\sigma_1^2} \quad \text{and} \quad w_2 = \frac{1}{2\sigma_2^2} \quad . \tag{11}$$

If the standard deviations are unknown, the minimization must also be done with respect to σ_1 and σ_2. The necessary conditions are:

$$\frac{\partial\lambda}{\partial\sigma_1} = 0 \quad \text{and} \quad \frac{\partial\lambda}{\partial\sigma_2} = 0 \quad . \tag{12}$$

If these conditions are fulfilled, one gets:

$$\sigma_1^2 = \frac{1}{n_1}\sum_{i=1}^{n_1}(d_{1,i} - G_{1,i}(\mathbf{m}))^2 \tag{13}$$

and

$$\sigma_2^2 = \frac{1}{n_2}\sum_{j=1}^{n_2}(d_{2,j} - G_{2,j}(\mathbf{m}))^2 \quad . \tag{14}$$

On inserting σ_1 and σ_2 from eqs. 13 and 14 into the expression of λ in eq. 10 and neglecting its constant part, the function will have the form:

$$\lambda = \frac{n_1}{2} \ln \left(\frac{1}{n_1} \sum_{i=1}^{n_1} (d_{1,i} - G_{1,i}(\mathbf{m}))^2 \right) + \frac{n_2}{2} \ln \left(\frac{1}{n_2} \sum_{j=1}^{n_2} (d_{2,j} - G_{2,j}(\mathbf{m}))^2 \right). \quad (15)$$

This function does not include σ_1 and σ_2. The next step is to find the minimum of λ, this being a function of the model parameters **m**. Once this minimum is found, it is the minimum with respect to σ_1 and σ_2 too, because of the constraints of eq. 12. Then the estimates of σ_1 and σ_2 can be calculated from eqs. 13 and 14. Their only further role is in the calculation of the standard deviations $\sigma(m_i)$, which measure the uncertainty of the model parameter estimates. As can be seen, there may be more than two tasks for which the evaluation in this way can be done jointly.

3. Numerical examples

3.1. Toy example

Numerical calculations were done to determine whether the method reproduces σ_1, σ_2 and **m** for a known model with reasonable accuracy. For task 1 and task 2 linear direct problems $\mathbf{G}_1(\mathbf{m})$ and $\mathbf{G}_2(\mathbf{m})$ — without any geophysical meaning — were created and n_m=5 model parameters were chosen whose exact numerical values are: m_1=1, m_2=2, m_3=3, m_4=4 and m_5=5. The $\mathbf{d}_1$ and $\mathbf{d}_2$ data were produced on the basis of eq. 1, where $\mathbf{e}_1$ and $\mathbf{e}_2$ are random samples from two univariate normal distributions of zero expected values with σ_1=1 and σ_2=10. In *Fig. 1* the curves show that the calculated standard deviations approximate the exact values of σ_1, σ_2 with increasing values of n_1 and n_2.

In the next example σ_1=1 and σ_2=10, and then σ_1=1 and σ_2=100 standard deviations were chosen respectively. The number of data are n_1=35, n_2=50. Because different tasks may depend on different parameters of the model, three cases, viz. α), β) and γ) were studied. In case α) task 1 and task 2 depend on all five model parameters; in case β), task 1 depends on m_1, m_2, m_3, m_4; task 2 depends on m_2, m_3, m_4, m_5. In case γ) task 1 depends on m_1, m_2, m_3; task 2 depends on m_3, m_4, m_5. It means that in cases

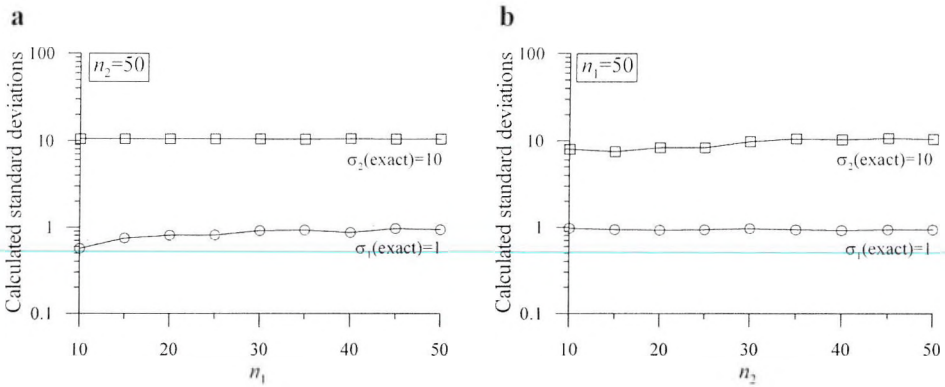

Fig. 1. Calculated standard deviations are plotted against the numbers n_1 and n_2. The exact standard deviations are σ_1(exact)=1 and σ_2(exact)=10. On graph a) n_2=50 while n_1 is increasing from 10 to 50, on graph b) n_1=50 and n_2 is increasing from 10 to 50

1. ábra. Számított standard szórás értékek függése az adatok n_1 és n_2 számától. A szórások egzakt értékei: σ_1(exact)=1 és σ_2(exact)=10. Az a) ábrán n_2=50, míg n_1 értéke 10 és 50 között változik. A b) ábrán n_1=50 és n_2 értéke változik 10 és 50 között

α) and β) there are respectively three and two common parameters, and for γ) there is one.

The uncertainty of the parameter estimates is measured by their standard deviations $\sigma(m_i)$ and by comparing the exact and the estimated values. The results are given in *Table I.* In each part of the table there are two inversion results: one for σ_1=1 and σ_2=10 and the other for σ_1=1 and σ_2=100. In cases α) all the model parameter estimates have almost the same standard deviations in spite of the fact that in the second example σ_2 is ten times greater than in the first example. In cases β) the estimates of m_1, m_2, m_3, and m_4 show almost the same standard deviations as in cases α), the standard deviation of m_5 is greater. The increase of σ_2 does not affect the standard deviations of m_1, m_2, m_3 and m_4, only the estimate of m_5 becomes even less accurate. In cases γ) the standard deviations of the estimates of m_1, m_2 and m_3 are approximately equal with those in cases α) and β). The standard deviations of m_4 and m_5 are greater and they are even greater for greater σ_2. Summarizing the results, one may conclude that the increase of σ_2 does not change the quality of the estimates of those model parameters which are variables of task 1, regardless of the fact that they may also be found in task 2. The increase of σ_2 causes a quality decrease for the estimates of parameters which are variables of task 2 exclusively.

a)

case α)	σ_1(exact)=1.0		σ_2(exact)=10.0		
n_1=35, n_2=50	σ_1(est)=0.960		σ_2(est)=10.46		
m(exact)	1.	2.	3.	4.	5.
m(est)	0.953	2.032	3.021	4.040	4.964
σ(**m**)	0.042	0.045	0.051	0.053	0.046
n_1=35, n_2=50	σ_1(exact)=1.0		σ_2(exact)=100.0		
case α)	σ_1(est)=0.959		σ_2(est)=104.8		
m(exact)	1.	2.	3.	4.	5.
m(est)	0.951	2.034	3.020	4.036	4.969
σ(**m**)	0.043	0.045	0.051	0.053	0.046

b)

case β)	σ_1(exact)=1.0		σ_2(exact)=10.0		
n_1=35, n_2=50	σ_1(est)=0.966		σ_2(est)=10.32		
m(exact)	1.	2.	3.	4.	5.
m(est)	0.939	2.030	3.011	4.035	4.770
σ(**m**)	0.040	0.045	0.049	0.051	0.147
n_1=35,n_2=50	σ_1(exact)=1.0		σ_2(exact)=100.0		
case β)	σ_1(est)=0.965		σ_2(est)=103.4		
m(exact)	1.	2.	3.	4.	5.
m(est)	0.941	2.033	3.011	4.030	3.288
σ(**m**)	0.040	0.045	0.049	0.051	1.424

c)

case γ)	σ_1(exact)=1.0		σ_2(exact)=10.0		
n_1=35, n_2=50	σ_1(est)=0.969		σ_2(est)=10.18		
m(exact)	1.	2.	3.	4.	5.
m(est)	0.947	2.038	3.023	4.451	4.415
σ(**m**)	0.038	0.044	0.043	0.364	0.352
n_1=35, n_2=50	σ_1(exact)=1.0		σ_2(exact)=100.0		
case γ)	σ_1(est)=0.969		σ_2(est)=101.8		
m(exact)	1.	2.	3.	4.	5.
m(est)	0.947	2.037	3.024	8.622	-0.773
σ(**m**)	0.038	0.044	0.044	3.633	3.516

Table I. a-c. Joint inversion results of two data sets for cases α), β) and γ). The table contains the numbers n_1 and n_2 of the data sets, the exact and estimated values of σ_1 and σ_2, the exact and estimated values of the model parameters **m**, and their standard deviations

I. a–c. táblázat. Két adatrendszer egyesített inverziós eredményei láthatók az α), β) és γ) esetekre. A táblázat tartalmazza az adatok n_1 és n_2 számát, a σ_1 és σ_2 standard szórások egzakt és becsült értékeit valamint az **m** modellparaméterek egzakt és becsült értékeit és azok standard szórásait

3.2. Joint inversion of gravity and magnetic data:

The gravity problem is task 1 and the magnetic problem is task 2. The geological object is a spherical body with homogeneous density and homogeneous intensity of magnetization. The radius of the body is $r = 50$ m. The mass of the sphere is $\Delta m = 2\text{x}10^8$ kg (=$2\text{x}10^5$ t), so the density of the sphere is 381.97 kg/m^3. The vertically oriented magnetic moment of the sphere is ΔM=$5\text{x}10^6$ Am^2, the intensity of magnetization is 9.549 A/m. The z axis of the rectangular coordinate system is directed downwards. The coordinates of the centre of the body are x_0=0, y_0=0 and z_0=100 m. Both the gravity and the magnetic data relate to the horizontal plane z=0. The Δg gravity anomaly is given in microgal units and the ΔB_z magnetic flux density anomaly is given in nT units. The theoretical model for gravity data is

$$\Delta g = G\frac{\Delta m}{r^2}\frac{z_0}{r} \quad , \tag{16}$$

where

$$r = ((x-x_0)^2 + (y-y_0)^2 + z_0^2)^{1/2}$$

which is the distance between the centre of the sphere and the point of observation, and G=6.673 *10^{-11} m^{3}kg^{-1}s^{-2} is the constant of gravitation. For magnetic data [PARASNIS 1979] the theoretical model is:

$$\Delta B_z = \frac{\mu_0}{4\pi}\frac{\Delta M}{r^3}\left(3\frac{z_0^2}{r^2} - 1\right) \quad . \tag{17}$$

In the above equation μ_0 is the magnetic permeability of the vacuum, $\mu_0 = 4\pi*10^{-7}$ VsA^{-1}m^{-1}.

The measuring area is a square containing 21*21=441 points, the distance between the neighbouring points is 10 m in both the x and y directions. The spherical body is below the centre of the square. The maximum theoretical anomaly values are 133.46 microgal and 1000 nT. At each point both gravity and magnetic data are measured. The unknown parameters of the model are mass Δm, magnetic moment ΔM, and the coordinates of the centre of the spherical body x_0, y_0 and z_0.

The erroneous $\mathbf{d}_1$ and $\mathbf{d}_2$ data were produced as in the earlier examples; the standard deviations for gravity and magnetic data are denoted by σ_{grav} and σ_{magn} respectively. Many inversion calculations were done for different

values of σ_{grav} and σ_{magn}. Two inversion results are shown in *Table II.* It is shown that the estimates of σ_{grav} and σ_{magn} approximate their exact values. The model parameter estimates and their standard deviations depend on the magnitude of σ_{grav} and σ_{magn}.

a	σ_{grav}(exact) = 5 μgal		σ_{magn}(exact) = 20 nT	
	σ_{grav}(est) = 5.22 μgal		σ_{magn}(est) = 20.44 nT	
parameter		exact	estimated	σ
Δm (t)		200000	199770	960
ΔM (Am^2)		5000000	4946600	30000
x_0(m)		0	–0.14	0.256
y_0(m)		0	0.07	0.256
z_0(m)		100	99.59	0.268

b	σ_{grav}(exact) = 10 μgal		σ_{magn}(exact) = 5 nT	
	σ_{grav}(est) = 10.53 μgal		σ_{magn}(est) = 5.06 nT	
parameter		exact	estimated	σ
Δm (t)		200000	201710	1400
ΔM (Am^2)		5000000	4989100	7990
x_0(m)		0	0.02	0.08
y_0(m)		0	–0.01	0.08
z_0(m)		100	99.93	0.07

Table II. a-b. Joint inversion results of simulated erroneous gravity and magnetic measurements. In the examples there are the exact and estimated values of the standard deviations σ_{grav} and σ_{magn}, the exact model parameters, their estimated values, and the standard deviations of the estimates.

II. a–b. táblázat. Példák hibával terhelt szimulált gravitációs és mágneses adatok egyesített inverziójára. A táblázatok tartalmazzák a σ_{grav} és σ_{magn} adatok egzakt és becsült értékeit, az egzakt és becsült modellparamétereket és a becsült paraméterek standard szórásait.

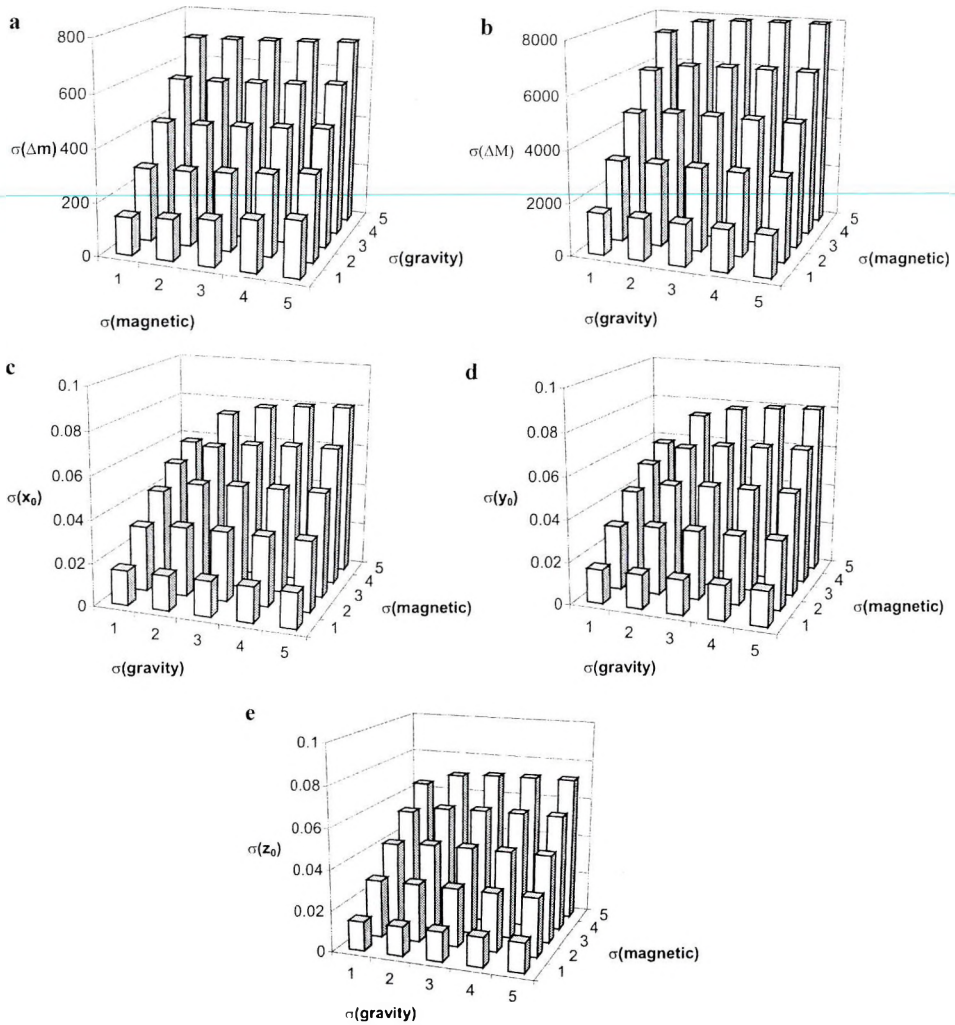

Fig. 2. Standard deviations $\sigma_{\Delta m}$, $\sigma_{\Delta M}$, σ_{x_0}, σ_{y_0} and σ_{z_0} are plotted on graphs a), b), c), d) and e) respectively for the values of σ_{grav} = 1, 2, 3, 4 and 5 μgal and σ_{magn} = 1, 2, 3, 4 and 5 nT. The graphs show the influence of σ_{grav} and σ_{magn} on the results of the joint inversion

2. ábra. Az a), b), c), d) és e) grafikonok a számított $\sigma_{\Delta m}$, $\sigma_{\Delta M}$, σ_{x_0}, σ_{y_0} és σ_{z_0} standard szórásoknak a σ_{grav} és σ_{magn} szórások nagyságától való függését mutatják σ_{grav} = 1, 2, 3, 4 és 5 μgal és σ_{magn} = 1, 2, 3, 4 és 5 nT értékek esetére

We should now like to deal with the problem how the standard deviations σ_{grav} and σ_{magn} influence the accuracy of the model parameter estimates. Systematic inversion experiments were done for σ_{grav}= 1, 2, 3, 4 and 5 microgal and σ_{magn}= 1, 2, 3, 4 and 5 nT. The standard deviations $\sigma(\Delta m)$, $\sigma(\Delta M)$, $\sigma(x_0)$, $\sigma(y_0)$ and $\sigma(z_0)$ are illustrated on plots **a**, **b**, **c**, **d** and **e** respectively in *Fig. 2.* The standard deviation $\sigma(\Delta m)$ shows essential dependence on σ_{grav}, the effect of σ_{magn} is relatively negligible. Similarly, $\sigma(\Delta M)$ depends essentially on σ_{magn} and the effect of σ_{grav} is negligible. The structure of plots **c**, **d**, **e** is similar to that of plot **b**, where stronger dependence on the geometrical parameters according to σ_{magn} than σ_{grav} can be seen. These examples show that in this special joint inversion problem the magnetic task produces a dominant influence on the estimates of the common parameters.

3.3. Joint inversion of penetration logs:

The evaluation of four penetration logs [FEJES, JÓSA 1990] is considered in this section: gamma ray (*GR*), density (*DEN*), neutron porosity (*FIN*), and resistivity (*R*). They are the four tasks of joint inversion. The model is a homogeneous soil layer consisting of water (V_w) and air (V_g) in the pore space, and a silica matrix (V_s) and clay (V_{cl}). There are *n* measuring depth points against the layer. The theoretical response functions of the logs [SERRA 1984] are:

$$GR = GR_s + V_{cl}\,(GR_{cl} - GR_s) \quad , \tag{18}$$

$$DEN = V_w + V_{cl}\,DEN_{cl} + (1 - V_w - V_g - V_{cl})\,DEN_s \quad , \tag{19}$$

$$FIN = V_w + V_{cl}\,FIN_{cl} \quad , \tag{20}$$

$$R = \left(\frac{V_{cl}}{R_{cl}} + \frac{V_w}{R_w} \right)^{-1} \frac{1}{(V_w + V_g + V_{cl})^{me-1}} \quad . \tag{21}$$

Eq. 21 is deWitte's shaly sand resistivity model [DEWITTE 1950], where *me* represents the cementation exponent. The constant zone parameters in the theoretical response functions and their numerical values are:

GR_{cl}=120 API unit, gamma ray intensity of clay,
GR_s=50 API unit, gamma ray intensity of sand,
DEN_{cl}=2.1 g/cm^3, density of clay,
DEN_s=2.65 g/cm^3, density of sand,
FIN_{cl}=0.3, neutron porosity of clay,
R_w=10 ohmm, resistivity of water,
R_{cl}=5 ohmm, resistivity of clay.

The exact model parameters are:

V_w=0.10, V_g=0.15, V_s=0.50 and V_{cl}=0.25.

For the *GR*, *DEN*, and *FIN* data, normal distribution is assumed; for the *R* data lognormal distribution is assumed. The standard deviations for producing the simulated erroneous data are: σ(*GR*)=10 API units, σ(*DEN*)=0.05 g/cm^3, σ(*FIN*)=0.05 and σ(log*R*)=0.11. *n*=20 erroneous data were produced. The results of the evaluation are shown in *Table III.* Comparison of the results shows convincing similarity between the original and the estimated quantities.

	GR	*DEN*	*FIN*	log*R*
σ(exact)	10.0 API	0.050 g/ccm	0.050 decim.	0.110 decim.
σ(est)	9.33 API	0.051 g/ccm	0.049 decim.	0.138 decim.
model	V_w	V_g	V_s	V_{cl}
m(exact)	0.100	0.150	0.500	0.250
m(est)	0.113	0.140	0.496	0.251
σ(**m**)	0.014	0.008	0.010	0.016

Table III. Joint inversion log evaluation example of gamma ray (*GR*), density (*DEN*), neutron porosity (*FIN*) and resistivity (*R*) penetration logs relating to a homogeneous soil layer. The parameters of the model are: water content (V_w) and gas content (V_g) of the pore space, the amount of silica (V_s) and clay (V_{cl}). There are the exact and the estimated standard deviations of the logs, the exact and estimated values of the model parameters and their standard deviations

III. táblázat. Hibával terhelt szimulált mérnökgeofizikai szelvények homogén talajréteg modellre vonatkozó egyesített inverziója. A figyelembe vett szelvények: természetes gamma (*GR*), sűrűség (*DEN*), neutron-porozitás (*FIN*) és fajlagos ellenállás (*R*). A talajmodell paraméterei: talajvíz (V_w) és levegő (V_g) mennyisége a pórustérben, homok (V_s) és agyag (V_{cl}) mennyisége. A táblázat tartalmazza a szelvények egzakt és becsült standard szórásait, a paraméterek egzakt és becsült értékeit valamint azok standard szórás értékekeit

3.4. Joint inversion of two refraction seismic data sets

Both task 1 and task 2 are simulated refraction seismic inversion problems. Two data sets $\mathbf{d}_1$ and $\mathbf{d}_2$ were recorded at the same measurement site therefore the same earth model is used for them. It is assumed that they show different normal error distributions which are characterized by σ_1=1 ms (good quality data) and σ_2=5 ms (poor quality data) standard deviations respectively. The number of data are n_1=20 and n_2=60. The model consists of two layers which are separated by a horizontal plane. The theoretical t travel time formulae [LOWRIE 2007] are:

$$t = \frac{x}{v_1} \quad \text{if} \quad x < x_i \qquad \text{and} \tag{22}$$

$$t = \frac{x}{v_2} + 2h\frac{\sqrt{v_2^2 - v_1^2}}{v_1 v_2} \quad \text{if} \quad x \geq x_i \quad , \tag{23}$$

where x_i is the crossover distance:

$$x_i = 2h\sqrt{\frac{v_2 + v_1}{v_2 - v_1}} \quad . \tag{24}$$

The exact parameters of the model are: v_1=300 m/s, v_2=600 m/s and the depth of the layer boundary is h=5 m. The geophones are situated along a line so that for task 1 the distances measured from the shot point are x_1=1 m, 2 m, 3 m,..., 20 m and for task 2 x_2=2 m, 4 m, 6 m, ..., 120 m respectively. The simulated erroneous data were produced as in the earlier examples. Four cases of inversion were done the results of which are in *Table IVa – d*:

case a): joint inversion for task 1 and task 2 according to equation 3 with w_1=w_2=1,

case b): joint inversion for task 1 and task 2 according to equation 15,

case c): separate inversion for task 1,

case d): separate inversion for task 2.

a) $n_1 = 20$ σ_1(exact) = 1 ms σ(est) = 3.62 ms		$n_2 = 60$ σ_2(exact) = 5 ms σ(est) = 3.62 ms	
parameter	exact	estimated	σ
v_1 (m/s)	300	293	8.8
v_2 (m/s)	600	590	7.2
h(m)	5	4.63	0.30

b) $n_1 = 20$ σ_1(exact) = 1 ms σ(est) = 0.99 ms		$n_2 = 60$ σ_2(exact) = 5 ms σ_2(est) = 5.65 ms	
parameter	exact	estimated	σ
v_1 (m/s)	300	300	2.1
v_2 (m/s)	600	594	5.5
h(m)	5	4.92	0.12

c) $n_1 = 20$ σ_1(exact) = 1 ms σ(est) = 0.99 ms		$n_2 = 0$	
parameter	exact	estimated	σ
v_1 (m/s)	300	300	2.0
v_2 (m/s)	600	417	68.0
h(m)	5	3.28	0.99

d) $n_1 = 0$		$n_2 = 60$ σ_2(exact) = 5 ms σ_2(est) = 5.60 ms	
parameter	exact	estimated	σ
v_1 (m/s)	300	287	19.5
v_2 (m/s)	600	590	8.7
h(m)	5	4.51	0.49

Table IV. a-d. The results of different inversion examples of two refraction seismic data sets are demonstrated. The tables contain the numbers of data n_1 and n_2, the exact and estimated standard deviations of the two data sets σ_1 and σ_2. There are the exact and the estimated values of the layer velocities v_1, v_2 respectively and those of the depth h of the boundary. The results are: usual joint inversion with equal weights (a), joint inversion according to equation 15 (b), and separate inversions of the two data sets (c) and (d)

IV. a–d. táblázat. A táblázatok két refrakciós adatrendszer inverziós eredményeit tartalmazzák. n_1 és n_2 a megfelelő adatszámok, σ_1 és σ_2 az adatrendszerek standard szórásai, v_1, v_2 a rétegek szeizmikus sebesség értékei, h a réteghatár mélysége. A táblázatokban a megfelelő mennyiségek egzakt és becsült értékei vannak négy inverziós megoldásra vonatkozóan: szokásos inverzió a (3) egyenlet szerint azonos súlyokkal (a), egyesített inverzió a (15) egyenlet szerint (b) és a két adatrendszer független inverziója (c) és (d)

In case a) the usual inversion strategy is used. Apparently there is no reason to apply weights because both data sets of task 1 and task 2 are seismic refraction travel times. In case b) the interpreter assumes that the quality of data may be different. Separate inversions of cases c) and d) were done to compare all the possible solutions. The best results (minimum standard deviations) were found for case b). Only the standard deviation of v_1 in case c) shows the same magnitude as in case b).

4. Conclusion

The proposed joint inversion method takes into consideration the 'forgotten part' of the likelihood functions. Optimization of the joint objective function relates not only to the unknown model parameters **m** but is extended to the unknown standard deviations. This is in accordance with the maximum likelihood principle, which asserts that the probability of observed data **d** is made as large as possible [MENKE 1989]. Optimization of the joint objective function according to the standard deviations of the data can be done analytically. This leads to a modified form of the joint objective function which depends only on the model parameters **m**. The method can be regarded as the generalization of the L_2 norm inversion technique. It is important to note that the data sets should be uncorrelated. The expression of the joint objective function of equation 13 can easily be utilized in the existing L_2 norm algorithm.

The simulated inversion examples dealt with relate to toy examples, gravity–magnetic joint inversion, log evaluation, and refraction seismic inversion. Based on experience the estimated standard deviations of the data approximate their exact values with a maximum of 10%–15% difference. To get this level of approximation the number of data in each task should be more than 10–15. The model parameter estimates approximate their known exact values with the degree measured by their calculated standard deviations. The example calculations show the influence of the data errors on the estimates of the common and uncommon model parameters of different tasks.

Acknowledgement

This research was supported by the Hungarian Scientific Research Fund (OTKA) under project No. T043748.

REFERENCES

DE NARDIS R., CARDARELLI E., DOBRÓKA M. 2005: Quasi 2D hybrid joint inversion of seismic and geoelectric data. Geophysical Prospecting **53**, 5, pp. 705–716

DEWITTE L. 1950: Relations between resistivities and fluid contents of porous rocks. Oil and Gas Journal Aug. 24, 1950

DOBRÓKA M., GYULAI Á., ORMOS T., CSÓKÁS J., DRESEN L. 1991: Joint inversion of seismic and geoelectric data recorded in an underground coal mine. Geophysical Prospecting **39**, pp. 643–665

FEJES I., JÓSA E. 1990: The engineering geophysical sounding method: Principles, instrumentation and computerized interpretation. *In:* S. H. WARD (Ed.): Geotechnical and Environmental Geophysics. vol. II: Environmental and Groundwater. Society of Exploration Geophysicists, Tulsa, OK, pp. 321–331.

JULIÀ J., AMMON C., HERRMAN R. B., CORREIG A. M. 2000: Joint inversion of receiver function and surface wave dispersion observations. Geophysical Journal International **143**, pp. 99–112

KENDALL M., STUART A. 1967: The Advanced Theory of Statistics. Charles Griffin and Company Limited, London 690 p.

LOWRIE W. 2007: Fundamentals of Geophysics. Second Edition. Cambridge University Press, Cambridge 381 p.

MENKE W. 1989: Geophysical Data Analysis: Discrete Inverse Theory. Academic Press, New York 289 p.

MOTA R., MONTEIRO SANTOS F. A. 2006: 2D sections of porosity and water saturation percent from combined resistivity and seismic surveys for hydrogeologic studies. The Leading Edge, **25**, 6, pp. 735–737.

PARASNIS D. S. 1979: Principles of applied geophysics. Chapman and Hall, London 274 p.

SERRA O. 1984: Developments in Petroleum Science 15. Fundamentals of well-log interpretation. The acquisition of logging data. Elsevier, Amsterdam 440 p.

TREITEL S., LINES R. 1999: Past, present and future of geophysical inversion – a Y2K analysis: CREWES Research Report – Volume 11 pp. 13–20

Az egyesített geofizikai inverzió célfüggvényeinek meghatározása

DRAHOS Dezső

Az egyesített inverzió megvalósítása során probléma a különböző geofizikai mérések adatrendszereihez tartozó súlyfaktorok megválasztása. Ezek az inverzió szükséges bemeneti paraméterei, amelyek általában nem ismertek, de a megoldás ezeknek is függvénye. Jelen dolgozatban egy olyan megoldást mutat be a szerző, amely alkalmazása során nem szükséges ismerni a súly-

faktorokat. A módszer lényege, hogy a maximum likelihood becslés során nemcsak a modellparaméterek szerint, hanem az adatok standard szórása szerint is optimalizálni kell a likelihood függvényt. A cikk geofizikai jelentés nélküli adatrendszerek, valamint szimulált, hibával terhelt geofizikai adatrendszerek együttes inverziós példáival illusztrálja a módszer alkalmazhatóságát.

ABOUT THE AUTHOR

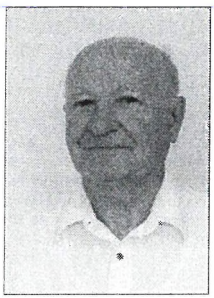

Dezső Drahos graduated as a geophysicist from the Eötvös Loránd University, Budapest in 1967. He received his Ph.D. degree from the Hungarian Academy of Sciences in 1989. From 1967 to 1970 he worked as a scientific associate at the Eötvös Loránd Geophysical Institute where he was involved in theoretical and experimental modelling of logging sondes. Since 1970 he has been at the Department of Geophysics of Eötvös Loránd University initially as a lecturer and, since 1991, as associate professor. Besides his teaching activities he is interested in geophysical inversion, well logging and petrophysics. He is a member of the Association of Hungarian Geophysicists, and also a member of EAGE, SEG and SPWLA.

GEOPHYSICAL TRANSACTIONS 2008
Vol. 45. No. 3. pp. 123– 134

Accuracy tests of LCR model G gravimeters

Géza CSAPÓ*

Due to the need for a more accurate geoid, in turn the necessity for a more refined gravity field with better resolution has been increased. Progress is being made by means of more accurate instruments using physical (particularly gravitational) observation techniques. Both torsion balance gradiometry and absolute gravimetry provide measurements with high accuracy; this high degree of accuracy can be supported by less accurate relative gravimetry by increasing the number of observation points. In this study measurements by recently used LCR gravimeters have been investigated under certain conditions of observation.

Keywords: accuracy, gravimeters, calibration, baseline, vertical gradient, gradiometry

1. Introduction

In recent years the need for a more accurate geoid has been increased, principally in order to increase positioning accuracy by GPS. This involves the necessity for a more refined knowledge of the gravity field with more delicate resolution. The investigations make use of observations based on both physical and geometrical considerations. Among the physical observation techniques, gravity measurements provide the best results. The observation instruments are super-conducting, absolute and relative gravimeters. Recently, investigations utilizing satellite gravimetry and gradiometry results have been taken into consideration [FUKUDA, FÖLDVÁRY 2001, TÓTH, FÖLDVÁRY et al. 2006]. As a means of increasing the efficiency of gravimetric observations, over the last few years transportable absolute gravimeters have been developed (cf. *Fig. 1*) that can also be used for field operations in view of which drastic improvements in the accuracy of terrestrial gravimetry can be expected. For μGal** and sub-μGal measurement accuracy by absolute and super-conducting gravimeters certain external disturbing effects should be taken into account, which have not

* Eötvös Loránd Geophysical Institute 1145 Budapest, Kolumbusz u. 17-23, Hungary

** $\mu Gal = 10^{-8} ms^{-2}$, $mGal = 10^{-5} ms^{-2}$

Manuscript received: 22 February, 2006

Fig. 1. Transportable absolute gravimeter at a field point

1. ábra. Szállítható abszolút graviméter egy terepi mérési ponton

been employed before except for theoretical studies. In order to study the structure of the gravity field, advantage is taken of the combined use of absolute and relative gravimeters. Although the measurement accuracy of these combined gravimeters is an order of magnitude smaller, they are suitable for providing additional information in a cost effective way for joint processing. It should be kept in mind that gravimetry is just a tool for gravity field investigations and it cannot replace geometric methods, i.e. levelling, GPS, or a knowledge of geology and hydrogeology. Reliable results can be derived only by employing physical and geometrical methods together, and interpreting all the available information in a complex, multiple way [CSAPÓ, VÖLGYESI 2005].

2. Interpretation of accuracy in gravimetry

Certain terms are used in gravimetry to describe the accuracy of a gravimeter. One of them is the so called 'inner accuracy'. First of all when simply 'accuracy' (or a posteriori accuracy) of a gravimeter is mentioned it refers to the standard deviation of Δg within a series of measurements. Often measurements between two points are done in A-B-A-B-A sequence, providing four different estimates for Δg. In this case the accuracy is defined by the standard deviation of the four estimates. This value primarily depends on the gravimeter, i.e. the properties of the instrument (including both random and systematic errors), subsequently on external disturbing effects and on the given observation method. There are also some external environmental effects, e.g. variations of the ground water and long-term gravity variations, though these have no effect on this accuracy estimate.

The so-called 'repeatability' term frequently used in gravimetry has a more practical sense. In this case the measurements are repeated in time, after some days, weeks or even years between the same two points and in the same manner. The measure for repeatability is then the standard deviation of the time series of the measurements. It is very important to know the repeatability of a gravimeter when time variations of the gravity field are studied, since it also depends, for example, on the time variations of the ground water content [VÖLGYESI et al. 2006].

3. Observation method used for accuracy tests of gravimeters

The instruments used were LCR–G gravimeters equipped with electronic levels owned by the Eötvös Loránd Geophysical Institute of Hungary (ELGI). Usually such instruments are used for high-precision measurements, e.g. for measuring the 'Unified European Gravity Network' (UEGN). The way in which dial readings are done depends on the structure of the gravimeter. In the case of older instruments, readings are carried out optically by turning the dial until the counter coincides with the so-called 'nulling counter'. With more up-to-date instruments a capacitive beam position indicator (CPI) is used to identify the counter, so the reading is done by turning the dial until the built-in galvanometer is set to zero. Both types of reading are referred to as the 'nulling method'. If the cables of the galvanometer can be connected to an external voltmeter, readings can be carried out in the so-called 'interpolating method'. In this case three different close-to-zero readings are taken simultaneously on the voltmeter and on the dial, and the exact reading is determined by interpolating the dial readings to the theoretical zero of the voltmeter. In this present study the interpolating method was used.

4. Determining the inner accuracy of the instrument by determining the true error of the measurement

In practice the true value of a measured quantity is not known, therefore neither is its true error. However, for gravimeters these can be determined by special arrangements of the measurements, e.g. if the two points of the observation tie are identical (i.e. A≡B), then the value of Δg between the 'two' points is known to be exactly zero. Therefore the deviation of the

measurements in an A–B–A–B–A sequence from zero should be considered to be the true error. Theoretically the calculated true error is not the error of the true value, since it contains all correction errors; however, for this test this difference can be neglected.

Test measurements were carried out at a point of the micro-baseline within one of Budapest's caves — the Mátyáshegy cave. Different sets of sequences were measured by altering the time interval between the measurements (A1, B1, A2, B2, A3) and the method of instrument transportation (on foot or by car), performing 3 series of measurements in each case. The readings were obtained by the 'interpolating method'. The height of the sensor mass inside the gravimeters above the micro-baseline point were determined with an accuracy of some mm, and the instruments were always set at the same azimuth. Atmospheric temperature and pressure were also measured. In the course of processing the measurements they were corrected for instrument height, also tidal and barometric corrections were taken into account, and the drift was removed. The time interval between the measurements was determined in the same way as is usually done in practice. Therefore when the transportation time of the gravimeters would have taken more than 20 minutes, it was done by car.

The results are shown in *Tables I–IV.* Observation accuracy depends on the time interval between the measurements and the method of transportation of the gravimeters [CSAPÓ 2002] (see bold values in Tables I–IV). These tables also show that the greatest deviations in most cases, either series with different gravimeters or measurements performed repeatedly with the same gravimeter, seldom exceed 10 μGal (cf. results of gravimeter number 963). By utilizing the value of the true errors a 'quality

series	measurements at the $\Delta g = 0$ tie; unit: mGal			
	LCR–1919	LCR–963	LCR–821	Δmax
1	– 0.0017	– 0.0049	+ 0.0019	0.0068
2	+ 0.0014	– 0.0027	+ 0.0019	0.0046
3	+ 0.0018	+ 0.0010	– 0.0017	0.0035
Δmax	0.0035	0.0059	0.0036	**0.0050**

Table I. Measurement results with transportation of the gravimeter on foot (measurement interval: $t = 10$ min)

I. táblázat. Mérési eredmények a graviméter kézi szállítása esetén: $t = 10$ perc

series	measurements at the $\Delta g = 0$ tie; unit: mGal			
	LCR–1919	LCR–963	LCR–821	Δmax
1	+ 0.0017	+ 0.0063	– 0.0029	0.0092
2	+ 0.0008	– 0.0016	+ 0.0030	0.0046
3	+0.0039	+ 0.0040	– 0.0012	0.0052
Δmax	0.0031	0.0079	0.0059	**0.0063**

Table II. Measurements with transportation of the gravimeter on foot (measurement interval: $t = 20$ min)

II. táblázat. Mérési eredmények a graviméter kézi szállítása esetén: $t = 20$ perc

series	measurements at the $\Delta g = 0$ tie; unit: mGal			
	LCR–1919	LCR–963	LCR–821	Δmax
1	+ 0.0017	+ 0.0053	+ 0.0028	0.0036
2	– 0.0052	+ 0.0024	+ 0.0058	0.0110
3	+ 0.0024	+ 0.0046	– 0.0010	0.0056
Δmax	0.0076	0.0029	0.0068	**0.0067**

Table III. Measurements with transportation of the gravimeter by car (measurement interval: $t = 20$ min)

III. táblázat. Mérési eredmények a graviméter gépkocsival történő szállítása esetén: $t = 20$ perc

series	measurements at the $\Delta g = 0$ tie; unit: mGal			
	LCR–1919	LCR–963	LCR–821	Δmax
1	+ 0.0046	– 0.0046	+ 0.0050	0.0096
2	+ 0.0024	+0.0020	– 0.0038	0.0062
3	+ 0.0034	+ 0.0032	+ 0.0065	0.0097
Δmax	0.0022	0.0078	0.0103	**0.0085**

Table IV. Measurements with transportation of the gravimeter by car (measurement interval: $t = 30$ min)

IV. táblázat. Mérési eredmények a graviméter gépkocsival történő szállítása esetén: $t = 30$ perc

order' can be established among these gravimeters. Note that the measurements were performed under ideal conditions, i.e. in the morning hours, when the temperature changes do not exceed 2–3° C. It is also mentioned that the choice of the station, i.e. inside a cave, provided a shielded, wind-free location.

Bearing in mind the results in Tables I-IV, we can conclude that when measuring vertical gradients indoors (i.e. absolute stations), or when deriving a gravity value for an eccentric point from an absolute station in the immediate vicinity, LCR–G gravimeters yield an accuracy of some μGals.

5. Determination of the accuracy of repeated measurements of the vertical gradient in two and in three positions

For relative gravimeter measurements made with repetition between field points the reliability of the measurement is evaluated in the interval (range) between the inner accuracy and the gross error. In the case of LCR gravimeters — judging from our experience — those measurements are regarded as gross errors where the differences of the corrected relative 'g' values, which can be calculated to the individual points from the measurements done in the same sequence, are higher than 0.03 mGal. Within the reliability range of the measurements, accuracy depends on external disturbing effects, the method of transportation of the instrument, and the distance between the two measurement points. In the case of repeated measurements with a longer period between measurements, further effects (mentioned in Section 2.) should be considered.

The term 'measurement of vertical gradient in two positions' refers to two observations of Δg at different heights at the same station. Accordingly, 'observation in three positions' refers to measurements at three levels along the plumb line. In this analysis A-B-A-B-A-B and A-B-C-B-A-B-C-B-A sequences were used respectively for the two positions' and three positions' solutions [CSAPÓ 2001; CSAPÓ, VÖLGYESI 2002]. By re-measuring the series later, the repeatability can be determined. Note that in the case of measurements of the vertical gradient, the range is always $\Delta g < 1$ mGal, therefore the relative accuracy decreases. These kinds of observations have been carried out both at indoor stations, e.g. absolute stations, and at field points in order to analyse the errors due to external disturbing effects. *Table V* shows the accuracy of vertical

Location	series	method	m_x by gravimeters			m_x (LCR all)
			LCR–821	LCR–963	LCR–1919	
at absolute stations						
Mátyás Cave	3	2 positions	± 0.0051	± 0.0025	± 0.0046	± 0.0046
Pecný	3	3 positions	–	± 0.0027	± 0.0028	± 0.0030
at field points						
Pécs airport	3	3 positions	–	± 0.0074	± 0.0048	± 0.0076
Műegyetem garden	3	3 positions	–	± 0.0107	± 0.0086	± 0.0097
Hármashatárhegy	3	3 positions	–	± 0.0108	± 0.0099	± 0.0109
Szépvölgyi street	3	3 positions	–	± 0.0065	± 0.0047	± 0.0064

Table V. Accuracy of vertical gradient measurements; unit: mGal
V. táblázat. A vertikális gradiens mérések pontossága mGal egységben

gradient measurements at a number of locations. The reliability of measurements with any specific gravimeter has been assumed to be the same. The mean of the measurements within a series has been assumed to be an independent observation. In Table V standard deviations were defined as the standard deviation of the mean of every series, i.e.:

$$m_x = \pm [(vv)/n\text{-}1]^{1/2}$$

It can be seen from Table V that observations at indoor (absolute) stations are twice as accurate as those at field points (cf. *Fig. 2*). In practice (i.e. for geophysical purposes) three series with two gravimeters at one point are rarely measured in view of which it should

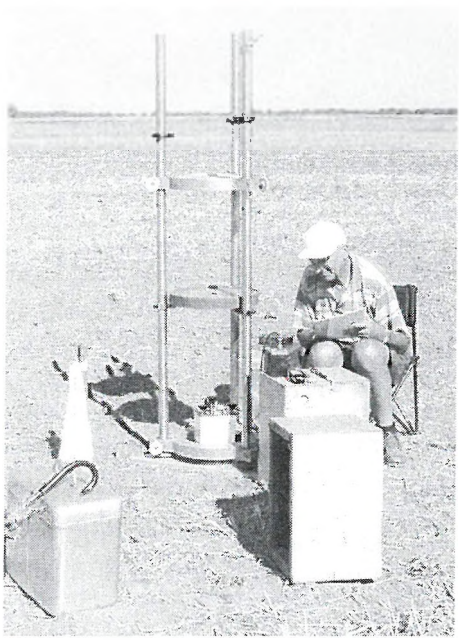

Fig. 2. Measuring vertical gradient at a field point
2. ábra. A vertikális gradiens mérése egy terepi ponton

be noted that this kind of analysis with one instrument would definitely provide less accurate results than given in this table.

The results show that not only are there random but also systematic deviations between the instruments. This resulted in a worse standard deviation for the combined adjustment (in the table 'LCR all') than from one gravimeter. Since, for so small measurements, differences in the scale factor of gravimeters have no effect on the result, these deviations can be interpreted with the differences of the periodic errors belonging to 1 mGal. The amplitude of periodic errors differs depending on the particular gravimeter. Empirically the error at 1 turn of the dial (cca. 1 mGal) was found to reach even 3–5 μGal.

6. Determination of repeatability by measurements on the national gravimeter calibration baseline

Most observations along the national calibration baseline (between Siklós and Szécsény with a range of about 210 mGal) were performed with the LCR–1919 gravimeter. In the following section these results are analysed. Calibrations have been done along this baseline for more than 20 years with a very experienced staff. In these investigations it is assumed that the scale factor of the gravimeters did not change beyond the accuracy of the measurements during the test period. Due to the long observation period neither the long-term variations of the gravity, nor ground water variations in the vicinity of the point, nor the change of the properties of the gravimeter (e.g. rheological characteristics of the gravimeter's spring) can be neglected. These effects are assumed to be involved in the deviations of the measurements.

The baseline belongs to three different geological structures therefore differences both in crustal movements and in hydrogeological properties should be expected. Observations at these observation ties are shown in *Table VI.*

The measurements at the neighbouring points of the baseline were performed in the aforementioned sequence, usually in early spring and/or in late autumn. During the processing, in all cases those corrections were applied that were mentioned in the section on accuracy determination. The

Table VI. Measurements on the calibration baseline between 1984 and 2004
VI. táblázat. Mérések 1984 és 2004 között a kalibrációs alapvonalon ⟹

date	81–101.10	101.10–102	102–103	103–104	104–4100	4100–106	106–107.10	107.10–82	82–4224	4224–4223
1984.12	15.790	45.016	36.434	16.456	3.274	28.204	33.985	(1.666)	8.152	20.535
1985.04	15.821	45.056	36.449	16.453	3.287	28.214	33.983	1.703	8.171	20.549
1986.04	15.820	45.039	36.473	16.452	3.266	28.218	33.987	1.695	8.171	20.548
1986.10	15.797	45.027	36.471	16.461	3.282	28.212	33.987	1.685	8.161	20.550 20.547
1987.03	15.792	45.031	36.464	16.445	3.284	28.234	33.992	1.670	8.184	20.556
1987.10	15.820	45.029 44.993	36.471	16.505	3.299	28.205	33.978	1.667	8.146 8.121	20.570
1988.04	15.814	45.040	(36.432)	(16.526)	3.267	(28.148)	(33.939)	(1.666)	8.146	20.536
1989.03	15.814	45.040	(36.432)	(16.526)	3.266	28.221	33.969	1.673	8.162	20.536
1989.10	15.807	45.044	36.440	16.424	3.267	(28.148)	(33.939)	(1.666)	8.146	20.536
1990.11	15.838	45.029	36.484	16.463	3.280	28.220	33.971	1.686	8.144	20.531
1991.04	15.820	45.035	36.466	16.463	3.278	28.220	33.965	1.691	8.154	20.544
1991.10	15.826	45.026	36.475	16.449	3.278	28.225	33.940	1.690	8.163	20.554
1992.03	15.823	45.034	36.472	16.444	3.292	28.230	33.968	1.688	8.174	20.544
1992.10	15.838	45.033	36.459	16.459	3.289	28.221	33.954	1.673	8.178	20.534
1993.03	15.811	45.040	36.470	16.437	3.284 3.279	28.213	33.966	1.706	8.184	20.542
1993.10	15.824	45.028	36.473	16.439 16.460	3.265	28.243	33.966	1.691	8.174	20.517
1994.10	15.822	45.040	36.460	16.455	–	28.224	33.965	1.675	8.170	20.532
1995.05	15.825	45.027	36.449	–	–	28.251	33.996	1.722	8.187	20.533
1998.06	(15.769)	(44.973)	36.493	–	–	28.217	33.968	1.697	8.172	20.555
2000.08	15.796	45.016	36.478	16.443	–	–	33.962	1.697	8.166	–
2001.03	15.794	45.024	36.485	–	–	–	33.959	1.730	8.195	–
2002.02	15.793	45.044	36.471	–	–	–	33.957	1.683	8.159	–
2003.04	15.803	45.053	36.444	–	–	–	(33.936)	1.697	8.152	–
2004.04	–	–	36.449	–	–	–	33.948	(1.666)	–	–
statistics for the whole data series										
mean	15.813	45.027	36.464	16.457	3.281	28.218	33.969	1.688	8.165	20.544
std. var	± 0.020	± 0.021	± 0.016	± 0.023	± 0.010	± 0.022	± 0.019	± 0.017	± 0.016	± 0.013
N	23	24	24	19	17	24	24	24	24	20
Δmax	0.092	0.083	0.061	0.102	0.034	0.103	0.067	0.064	0.074	0.053
statistics for the filtered data (non-normal distribution checked by χ^2 test)										
mean	15.813	45.032	36.465	16.453	3.281	28.224	33.970	1.691	8.165	20.544
std. var	± 0.015	± 0.013	± 0.015	± 0.017	± 0.010	± 0.012	± 0.015	± 0.016	± 0.016	± 0.013
N	23	23	22	17	17	22	21	20	24	20
Δmax	0.071	0.063	0.059	0.081	0.034	0.047	0.056	0.063	0.074	0.053

observations were adjusted in the Least Squares sense by the Danish iteration method on the basis of a fixed network. The constraints of the adjustment were defined to be the gravity acceleration values of points 81 and 82 determined in the year 1990, regardless of whether at the absolute stations repeated determinations before or after 1990 had been performed. (These repeated absolute determinations were taken into account with the relative measurements). Daily means of Δg values of neighbouring points were assumed to be independent observations.

Table VI shows the date of the observations (year/month) with the measured Δg values without a sign at the observation ties in mGal units. The observation ties are labelled with the catalogue numbers of the stations. Some statistics of the Δg measurements were calculated (mean, standard deviation), and are shown in the table along with the number of observations (N) and with the maximum deviation during the 20 years' period (Δ_{max}). For those observation ties where $N \geq 15$, a normality test was performed using the χ^2 test. At a confidence level of 0.997 (i.e. 3σ) all the measurements were found to follow normal distribution; even at a confidence level of 0.92 only a few data were rejected — these values are shown in parentheses in the table.

From the tests it can be concluded that

—*There is no correlation between the amplitude and the standard deviation of the observation.* The standard deviations are between ± 0.010 and 0.023 mGal depending on the number of observations; on average ± 0.016 mGal.

—*No definite correlation between the amplitude of the observation and* Δ_{max} *was found.*

On the other hand, it is obvious that Δ_{max} values are notably larger than the corresponding standard deviations. *This suggests that repeatedly measured* observation ties *(with a long duration between the measurements) can provide fairly different* Δg*, which differences are not a consequence of accuracy-decay of the instrument, but of different external effects and of variations in the gravity field.* The difference in values is certainly important for fundamental gravity networks. In cases of national basic gravity networks the measuring campaign can take some years, and — since meanwhile temporal variations of the gravity field are not uniform — the accuracy of the network unavoidably decreases. Due to these temporal variations (and other, additional reasons) the national fundamental networks should be re-measured every 10–15 years. In the new networks

more and more absolute stations are established (the so-called 0^{th} order network), re-measurement of these stations also enables stability control of the whole network. With the increase in number of the absolute stations, local networks become more inexpensive. Further investigations on the geological aspects of these measurements carried out on the national calibration baseline are planned to be discussed in a separate paper.

Acknowledgement

Most of the measurements for this study were financed by the Hungarian Scientific Research Fund (OTKA) grant numbers T037929 and T60657.

REFERENCES

CSAPÓ G. 2001: Vertical gravity gradient (VG) — its measurement methods and its role in high accuracy gravimeter measurements (in Hungarian). Mérésügyi Közlemények **XVII**, 2001/3, pp. 67–72

CSAPÓ G. 2002: Investigation of the condition systems of high accuracy geodetical-gravimetric measurements and practical adaptation of the results (in Hungarian). Doctoral thesis, Budapest

CSAPÓ G., VÖLGYESI L. 2002: Determination and reliability estimation of vertical gradients based on test measurements. 3rd Meeting of the International Gravity and Geoid Commission (IAG Section III.), Thessaloniki, Greece.

CSAPÓ G., VÖLGYESI L. 2005: Application of geodetic and geophysical methods for examining the time of gravity (in Hungarian). Geomatikai Közlemények **VIII**. pp. 193–200. Sopron

FUKUDA Y., FÖLDVÁRY L. 2001: Environmental corrections for the precise gravity observations by mean of satellite gravity data. Journal of the Geodetic Society of Japan **47**, 2, pp.: 679–685 (in Japanese with English abstract).

TÓTH Gy., FÖLDVÁRY L., TZIAVOS I. N., ÁDÁM J. 2006: Upward/Downward Continuation of Gravity Gradients for Precise Geoid Determination. Acta Geodetica et Geophysica Hungarica **41**, 1, pp. 21–30.

VÖLGYESI L., TÓTH Gy., CSAPÓ G., SZABÓ Z. 2006: Investigation of non-tidal variations of gravity (in Hungarian). Geomatikai Közlemények **IX**, pp. 110–121

Geodéziai típusú LCR graviméterek pontossági vizsgálata

CSAPÓ Géza

Az egyre pontosabb geoid előállításának igénye miatt megnőtt a nehézségi erőtér részletesebb — és nagyobb felbontású — ismeretének szükségessége. A feladat megoldását segíti a fizikai alapú mérési módszerek, elsősorban a gravitációs módszerek alkalmazása — egyre nagyobb megbízhatóságú műszerek igénybe vételével. Az Eötvös ingával végzett gradiensmérések és az abszolút módszerrel végrejhatjott nehézségi gyorsulás meghatározások nagy megbízhatóságú eredményeket szolgáltatnak, de a földi mérési pontok számának növelése a kevésbé pontos relatív graviméteres mérésektől sem tekinthet el. A dolgozatban ma használatos LCR graviméterek különböző mérési körülmények között végzett mérési eredményeinek megbízhatóságát vizsgáltuk.

ABOUT THE AUTHOR

Géza Csapó graduated as a geodesist from the Technical University of Budapest in 1966. He then joined ELGI and specialized in gravimetry. In 1975 he was awarded a postgraduate degree and, in 1984, his Ph. D. — both of them in gravimetry. From 1970 to 1990 he carried out gravity measurements in many European countries, in South America and in Mongolia. At present he is principal scientific officer in the Earth Physics Department of ELGI. In 2004 he was awarded his D.Sc. degree by the Hungarian Academy of Sciences. His main fields of interest are high precision gravimetry, instrument development, and calibration.

GEOPHYSICAL TRANSACTIONS 2008
Vol. 45. No. 3. pp. 135– 156

Modelling and examination of penetration neutron sonde behaviour in various logging environments by Monte Carlo method and diffusion approximation

László BALÁZS*

Calculations of the neutron log response in different logging environments require solution of the relevant transport equation under the same conditions as those of the theoretical measuring model. To study the behaviour of a neutron sonde, special series of theoretical logging models with varying parameters have to be applied; these need to be suitable for examining spatial sensitivity (investigation depth, vertical resolution). The source of the given neutron field was a pointwise Am-Be source.

In this article the radial sensitivity function ('geometric factor') and vertical sensitivity function were calculated, and some important calibration curves were also derived. The calculations were carried out by the Monte Carlo method and two-group diffusion approximation.

Keywords: neutron logging, Monte Carlo method, perturbation

1. Introduction

The modelling of conventional neutron log measurement (direct problem) in a given medium requires the solution of the stationary transport equation. This partial differential equation — in relation to the neutron flux (φ) in an appropriate phase space (position ($\mathbf{r}$), solid angle ($\mathbf{\Omega}$) and energy (E)) — is the following:

$$0 = \mathbf{\Omega}\nabla\varphi(\mathbf{r}, E, \mathbf{\Omega}) - \Sigma_t(\mathbf{r}, E)\varphi(\mathbf{r}, E, \mathbf{\Omega}) + Q(\mathbf{r}, E, \mathbf{\Omega}) \qquad (1)$$

where:

Σ_t: macroscopic total cross section

Q: general source term

This general source term consists of two parts, viz. external source and scattered part [STACEY 2001, SZATMÁRY 2000]:

* Eötvös Loránd University, Faculty of Science, Institute of Geography and Earth Sciences, Department of Geophysics, 1117 Budapest, Pázmány P. sétány 1/C Hungary. e-mail: laszlo_balazs_61@freemail.hu

Manuscript received: 22 January, 2007

$$Q(\mathbf{r}, E, \mathbf{\Omega}) = \int_{4\pi}\int_{0}^{\infty} \Sigma_s(\mathbf{r}, E' \to E, \mathbf{\Omega}'\mathbf{\Omega})\, \varphi(\mathbf{r}, E', \mathbf{\Omega}')\, dE' d\mathbf{\Omega}' + S(\mathbf{r}, E, \mathbf{\Omega}') \quad (2)$$

where:

Σ_s : differential macroscopic scattering cross section

$S(\mathbf{r}, E, \mathbf{\Omega})$: external neutron source, inhomogeneous term of transport equation.

The external source in our approximation is a point source with isotropic angle distribution:

$$S(\mathbf{r}, E) = \delta(\mathbf{r} - \mathbf{r}_s)\ . \quad (3)$$

This equation can be solved by the Monte Carlo method or any other approximation of the transport equation, for example by the diffusion method. (The diffusion equation can be derived by expansion and integration of the transport equation using the solid angle.)

The diffusion equation in our case is the following:

$$0 = \nabla\big(D(E, \mathbf{r})\nabla\varphi(\mathbf{r}, E)\big) - \Sigma_t(\mathbf{r}, E)\, \varphi(\mathbf{r}, E) + Q(\mathbf{r}, E)\,. \quad (4)$$

After discretization of the energy variable, the coupled multi-group diffusion equation system can be achieved (system of Helmholtz equations).

$$D_i \Delta\varphi_i(\mathbf{r}) - \Sigma_{r,i}\varphi_i(\mathbf{r}) + \sum_j \Sigma_{r,j\to i}\varphi_j(\mathbf{r}) = S_i(\mathbf{r}) \qquad i, j : 1...n \quad (5)$$

where:

n: number of energy group,

D_i : diffusion coefficient in energy group *i*.

Σ_i: removal cross section in energy group *i*.

$\Sigma_{i,j}$: scattering cross section from *i*-th energy group to *j*-th.

In order to derive the coefficient of the equation (group constants) a neutron spectrum is required as a weighting function. The external source is a pointwise Am–Be source. The energy spectrum of this source is displayed in *Fig.1* [KNOLL 1989].

The neutron detection process (^{3}He(n,p)^{3}T) in the ^{3}He gas-filled proportional detector is not modelled. The reaction rate is regarded as being proportional with the local thermal neutron flux.

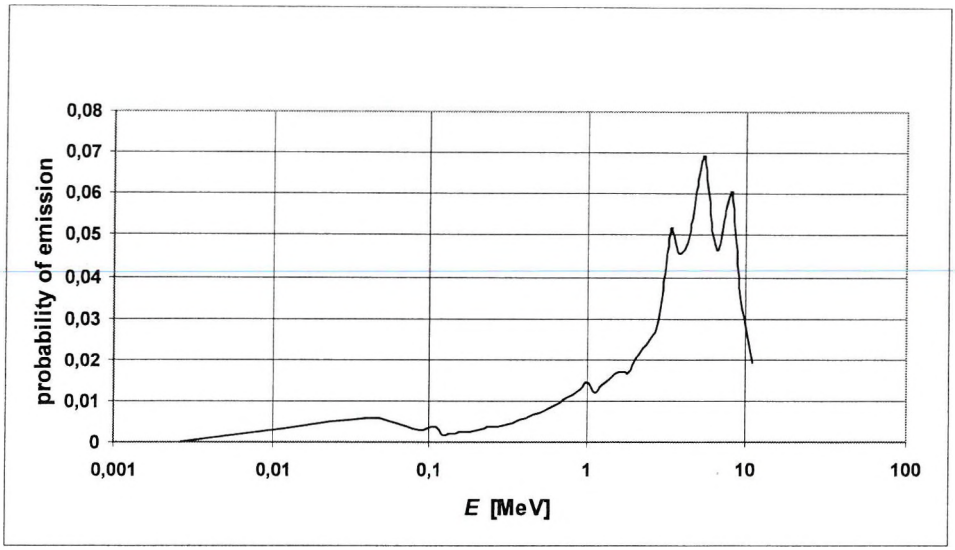

Fig. 1. Energy spectrum of Am–Be neutron source
1. ábra. Am–Be neutronforrás energiaspektruma

For a description of spatial sensitivity (importance), it should be determined how the count rate of the neutron sonde depends on the local perturbation of the embedding medium. Perturbation means the local variation of cross sections. In our study the porosity and density are perturbed.

This problem is not linear because the effect of perturbation is relatively complex. It has an influence on local absorption as well as on neutron moderation (scattering). It may disturb that part of neutron transport which is scattered back from the outer region. Therefore the sensitivity map, which is independent of the measured medium, cannot be derived; instead, only a series of rock dependent maps can be calculated to determine the radial and vertical resolution of the sonde or, otherwise, the average investigation depth can be determined.

2. Perturbation method

In the course of the sensitivity study, it is assumed that there is local perturbation in the homogeneous rock thereby enabling us to examine its effect in the detector response. The geometry of the measurement can be seen in *Fig. 2*. The assumed perturbation is located in a small volume,

where the transport properties (cross sections) differ from the properties of the embedding rock.

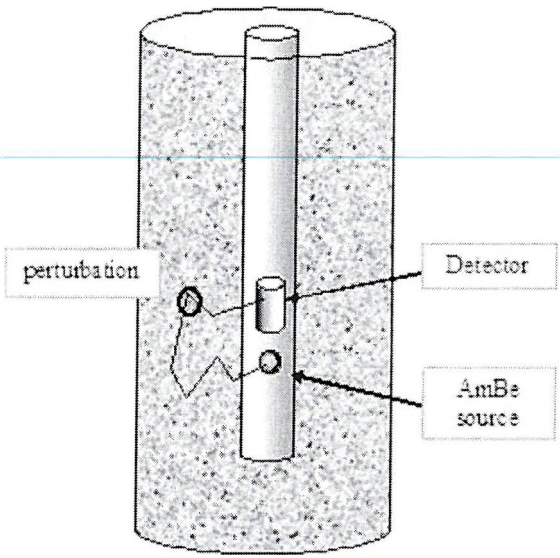

Fig.2. First model of measurement
2. ábra. Az első mérési modell

This perturbation causes perturbation in the neutron flux field, which decreases with distance as we move away from the position of perturbation. Thus, the perturbed transport (**T**) operator can be expressed in the form [ARFKEN, WEBER 1995]:

$$\mathbf{T} = \mathbf{T}_0 + \lambda\delta\mathbf{T} \tag{6}$$

where:

$\mathbf{T}_0$: unperturbed transport operator (describes the case of homogeneous rock)

$\delta\mathbf{T}$: perturbation operator (vanishes outside the perturbed region)

λ: measure of perturbation.

If the basic solution of the transport equation in a given approximation is known, the unperturbed neutron flux (φ_0) around the source (S) can be calculated as well as the detector response

$$\mathbf{T}_0\varphi_0 = S \quad . \tag{7}$$

If perturbation exists, the transport equation for the perturbed flux is given by:

$$\mathbf{T}\varphi = (\lambda\delta\mathbf{T} + \mathbf{T}_0)(\varphi_0 + \lambda\delta\varphi + \lambda^2\delta\varphi_2 + ...) = S. \tag{8}$$

Neglecting the small (higher order) terms:

$$\lambda\delta\mathbf{T}\varphi_0 + \mathbf{T}_0\varphi_0 + \lambda\mathbf{T}_0\delta\varphi_0 = S \tag{9}$$

$$\delta\mathbf{T}\varphi_0 = -\mathbf{T}_0\delta\varphi_1 = -\mathbf{T}_0\delta\varphi \ . \tag{10}$$

The index of perturbed flux is neglected to avoid any confusion with the energy group index. The equation for perturbed flux is inhomogeneous. The inhomogeneous term can be expressed by unperturbed flux and the perturbation term of the transport operator. As it can be seen, the goal of the perturbation procedure is to get a simpler equation for the perturbed flux which depends on the unperturbed operator, and only the inhomogeneous term of equation depends on the unperturbed operator.

So this method is also useful for mapping the spatial sensitivity of the detector, placing local perturbation to a different position.

3. Perturbation effect in diffusion approximation

Using the Green-function ($G(\boldsymbol{r})$) of the diffusion (Helmholtz) operator, the solution can be calculated by convolution:

$$\delta\varphi = -G * \delta\mathbf{T}\varphi_0 \ . \tag{11}$$

In that the perturbation operator vanishes outside the perturbation region, the inhomogeneous term can be achieved relatively easily.

In multi-group approximation — using such a kind of group structure that allows the up-scattering to be neglected — the equation of the highest energy group is independent of the others. The group fluxes can be derived step by step starting from the highest energy group.

To calculate the detector response the thermal flux has to be derived since the detectors are generally sensitive almost only in the thermal energy region because of the cross section-energy function of the ^{3}He

nucleus. The equations in two group approximation in the unperturbed case are [KISS, QUITTNER 1971, SZATMÁRY 2000]:

$$D_1\Delta\varphi_1(\mathbf{r}) - \Sigma_{r1}\varphi_1(\mathbf{r}) = S(\mathbf{r}) \tag{12a}$$

$$D_2\Delta\varphi_2(\mathbf{r}) - \Sigma_{r2}\phi_2(\mathbf{r}) + \Sigma_{r1}\varphi_1(\mathbf{r}) = 0 \tag{12b}$$

where:

D_i : diffusion coefficient in energy group i.

Σ_{ri} : removal cross section in energy group i.

φ_i : neutron flux in energy group i.

After the small material perturbation in ($\mathbf{r}_p$), the equations will be the following:

$$(D_1 + \delta D_1)\Delta(\varphi_1 + \delta\varphi_1) - (\Sigma_{r1} + \delta\Sigma_{r1})(\varphi_1 + \delta\varphi_1) = S(r) \tag{13a}$$

$$(D_2 + \delta D_2)\Delta(\varphi_2 + \delta\varphi_2) - (\Sigma_{r2} + \delta\Sigma_{r2})(\varphi_2 + \delta\varphi_2) + (\Sigma_{r1} + \delta\Sigma_{r1})(\varphi_1 + \delta\varphi_1) = 0 \tag{13b}$$

It should be noted that the sign of δD and of $\delta\Sigma$ are, in general, opposite in the case of material perturbation (e.g. local porosity variation). Neglecting the higher order terms, the equation for epithermal flux is given by

$$D_1\Delta\delta\varphi_1 - \Sigma_{r1}\delta\varphi_1 = \delta\Sigma_{r1}\varphi_1 - \delta D_1\Delta\varphi_1 = \left(\delta\Sigma_{r1} + \frac{\delta D_1}{D_1}\Sigma_{r1}\right)\varphi_1 \ . \tag{14}$$

The source term of the epithermal flux equation can be expressed by the unperturbed epithermal flux. With similar approximation the equations for the perturbed thermal flux are:

$$D_2\Delta\delta\varphi_2 - \Sigma_{r2}\delta\varphi_2 + \Sigma_{r1}\delta\varphi_1 = \delta D_2\Delta\varphi_2 + \delta\Sigma_{r2}\varphi_2 - \delta\Sigma_{r1}\varphi_1$$

$$D_2\Delta\delta\varphi_2 - \Sigma_{r2}\delta\varphi_{21} = \left(\frac{\delta D_2}{D_2}\Sigma_{r2} + \delta\Sigma_{r2}\right)\varphi_2 - \left(\frac{\delta D_2}{D_2}\Sigma_{r1} + \delta\Sigma_{r1}\right)\varphi_1 - \Sigma_{r1}\delta\varphi \ . \tag{15}$$

The perturbed thermal flux is determined by the following elements:

— the diffusion of perturbed thermal flux

— the absorption of perturbed thermal flux

— thermalization of epithermal flux.

It should be noted that if equation 4 is used to achieve the perturbation equation, a further term appears in the inhomogeneous part of the equation that is proportional to the volume of the perturbed region.

Since in the first order of perturbation:

$$\nabla((D+\delta D)\nabla(\varphi+\delta\varphi))-(\Sigma_1+\delta\Sigma_1)(\varphi+\delta\varphi)+S=0 \quad . \tag{16}$$

After some manipulations:

$$D\Delta\delta\nabla\varphi-\Sigma_1\delta\varphi=-\nabla\delta D\nabla\varphi+\delta D\Delta\varphi+\delta\Sigma_1\varphi \quad . \tag{17}$$

If Taylor expansion is applied for the small perturbed region the first term of the inhomogeneous part can be expressed by

$$\nabla\delta D\nabla\varphi=-2V_p\delta D\Delta\varphi \tag{18}$$

where V_p is the volume of perturbed region.

In the further calculation this term is neglected assuming the perturbed region to be very small.

The solution for the perturbed epithermal flux — which vanishes in infinity — can be expressed in convolutional form, as was mentioned above.

$$\delta\varphi_1(\mathbf{r})=\left(\delta\Sigma_{r1}+\frac{\delta D}{D_1}\Sigma_{r1}\right)\varphi_1(\mathbf{r}_p)\frac{e^{-|\mathbf{r}-\mathbf{r}_p|/Ls}}{4\pi D_1|\mathbf{r}-\mathbf{r}_p|} \quad . \tag{19}$$

The inhomogeneous term of the thermal flux equation can be separated into two parts: the first part vanishes outside the perturbation region, so this part can be approximated by a point source; the second part generates a similar solution as it was in the thermal group in the unperturbed case.

The sum of the two types of solution is:

$$\begin{aligned}\delta\varphi_2(\mathbf{r})=&\frac{L^2}{4\pi D_2(Ls^2-L^2)}\left(\delta\Sigma_{r1}-\frac{\delta D_1}{D_1}\Sigma_{r1}\right)\varphi_1(\mathbf{r}_p)\left[\frac{e^{\frac{-|\mathbf{r}_p-\mathbf{r}|}{Ls}}-e^{\frac{-|\mathbf{r}_p-\mathbf{r}|}{L}}}{|\mathbf{r}_p-\mathbf{r}|}\right]+\\&+\left\{\left(\delta\Sigma_{r2}-\frac{\delta D_2}{D_2}\Sigma_{r2}\right)\varphi_2(\mathbf{r}_p)-\left(\delta\Sigma_{r1}-\frac{\delta D_2}{D_2}\Sigma_{r1}\right)\varphi_1(\mathbf{r}_p)\right\}\frac{1}{4\pi D_2}\frac{e^{-|\mathbf{r}-\mathbf{r}_p|/L}}{|\mathbf{r}-\mathbf{r}_p|}\end{aligned} \tag{20}$$

where:

L: diffusion length

L_s: slowing down length

r_p: detector position
δD: perturbed diffusion coefficient
$\delta\Sigma_t$: perturbed total macroscopic cross section.

It can be seen that the perturbation vanishes as the perturbed coefficient tends to zero. If the thermal flux in the detector volume is calculated as a function of perturbation position, a spatial sensitivity map (spatial importance of the medium) would be generated $(\varphi(\mathbf{r}_d, \mathbf{r}_p, \delta\Sigma_i))$.

In the modelling (in our example) the source coordinates were ($r = 0$, $z = 12$) in the cylindrical coordinate system, and the detector coordinates were ($r = 0$, $z = 14...24$). To study the perturbation effect 10% perturbation is assumed.

The case of 20% porosity sandstone can be seen in *Fig. 3,* where the perturbation was 22% sandstone. In Figs. 3 and 4 the absolute values of group flux perturbation are displayed as a function of perturbation position. In other words, an importance map is generated which shows the importance of an infinitesimal volume at a given location (r, z) from the point of view of detector response. Normalizing with the integral of flux perturbations according to r and z the relative importance values are achieved.

From the figures (*Figs. 3 and 4*) it can be seen that the sensitivity map of the thermal flux is asymmetric at the detector. If the porosity of perturbation is higher than that of the embedding rock, then the perturbation causes a negative effect in the measured thermal flux if the position is close to the source and positive if it is close to the detector. If the perturbed region has a lower porosity, then the effect is the opposite. In the case of lower porosity rock the sensitivity decrease is less pronounced.

It should be noted that due to the finite measuring time, the perturbation effect could be smaller than the statistical fluctuation of the measured count rate. This effect also limits detection of the perturbation effect, and also limits the depth of investigation.

The finite measure of the detector is taken into account by integrating the perturbation effect for all detector volumes.

If the detection process is also treated, the adjoint flux is necessary for determining the count rate perturbation. In this case the source of the adjoint flux equation is the ^{3}He(n,p) ^{3}T reaction cross section, which is located in the space within the ^{3}He neutron detector tube. In this approximation the product of direct and adjoint flux gives the spatial sensitivity [SZATMÁRY 2000].

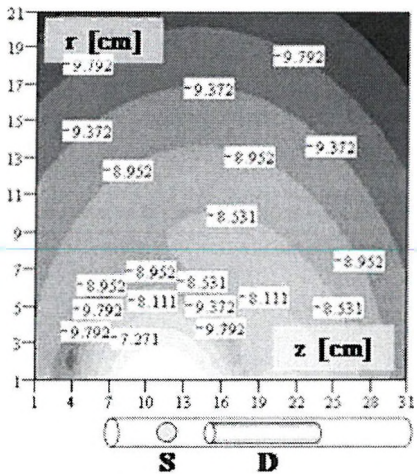

Fig.3. Relative importance map for 20% porosity sandstone, that is the thermal flux perturbation (absolute value on logarithmic scale) at the detector as a function of perturbation location. Near the source (**S**) large negative contribution can be identified because of the shielding dominance whereas around the detector (**D**) a smaller positive region exists as a result of stronger thermalization.

3. ábra. Relaitv fontossági eloszlás 20% porozitású homokkőre, azaz a termál fluxus perturbációja a detektornál (abszolút érték logaritmikus skálán) a perturbáció helyének függvényében. A forrás (**S**) közelében nagy negatív érték azonosítható az árnyékolás dominanciája miatt, míg a detektor (**D**) körül egy kisebb pozitív tartomány létezik az erősebb termalizáció következtében

The spatial distribution of the perturbed flux for pointwise perturbation can be approximated by a point neutron source field (an example can be seen in *Fig. 5).*

By integrating the spatial distribution function, radial and vertical sensitivity functions can be generated (geometric factors) (*Figs. 6 and 7).*

It can be seen that the maximum of curves does not vary essentially with the detector–source distance. The meaning of negative values is that the shallow region effect is dominantly the shielding.

The vertical sensitivity may be examined in a similar way: by integrating the perturbation effect along the thin vertical layer.

4. Monte Carlo study of sonde sensitivity

Radial sensitivity, which reflects the research depth, can be derived by the Monte Carlo method as well (using the MCNP code). With the Monte

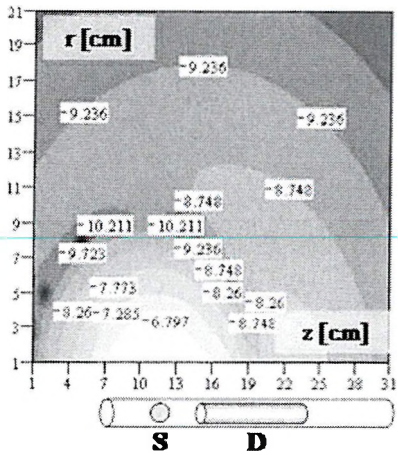

Fig.4. Relative importance map for 10% porosity sandstone. Thermal flux perturbation (absolute value on logarithmic scale) at the detector as a function of perturbation location. The importance distribution is very similar to that in Fig. 3, but the decrease is less pronounced than in the previous case.

4. ábra. Relaitv fontossági eloszlás 10% porozitású homokkőre, azaz a termál fluxus perturbációja a detektornál (abszolút érték logaritmikus skálán) a perturbáció helyének függvényében. A fontossági eloszlás nagyon hasonló a 3. ábrán látható képhez, de a csökkenés kevésbé hangsúlyos, mint az előző esetben

Carlo method the flux anisotropy and spectral changes are automatically taken into account. The finite detector volume is also easily taken into account since the Monte Carlo type flux determination is based on the neutron path summation in detector volume.

In *Figs. 8a* and *8b*, the spatial spectrum variation can be followed around the Am–Be source in 20% porosity sandstone. It should be noted that the group coefficient in multi-group diffusion approximation can be calculated by spectral weighting so the spectral changes must be taken into account. The microscopic cross sections originate from the ENDF VI [2001] library.

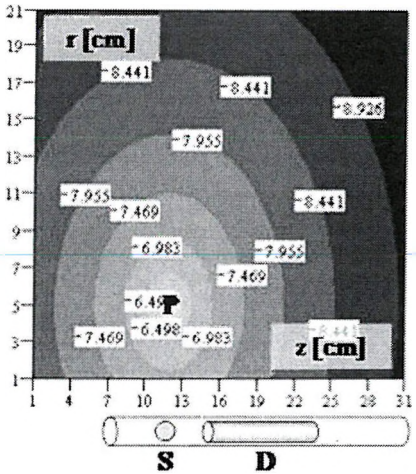

Fig. 5. Perturbed neutron flux field around an infinitely small perturbation centre (**P**) embedded in 22% porosity sandstone. Similarly to Figs. 3 and 4, on the *x* axis the vertical distance (*z*) is displayed and on the *y* axis the radial distance. The perturbed small volume is located at the coordinates (12, 5)

5. ábra. Perturbált neutron fluxus tér egy végtelenül kicsiny perturbációs központ (**P**) körül, 22% porozitású homokkőbe ágyazva. Hasonlóan a 3. és 4. ábrákhoz, az *x* tengelyen a függőleges távolságot (*z*), az *y* tengelyen a sugárirányú távolságot ábrázoltuk. A perturbált kis térfogat a (12, 5) koordinátáknál található

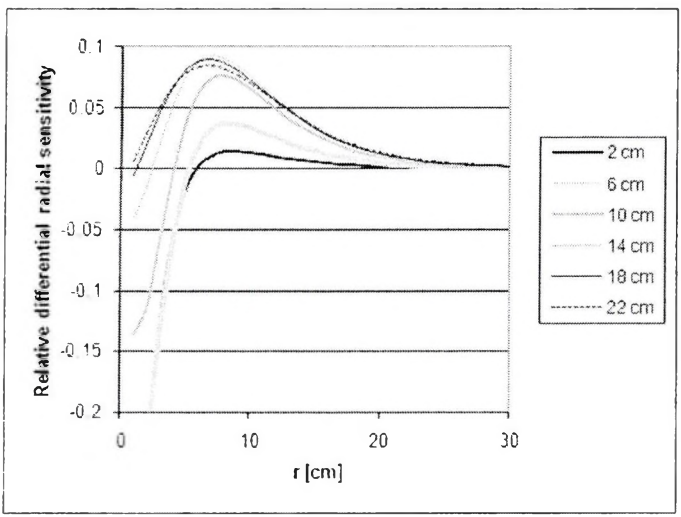

Fig. 6. Relative differential radial sensitivity functions in 20% porosity sandstone at various detector–source distances (curve parameter).

6. ábra. Relatív differenciális sugárirányú érzékenység 20% porozitású homokkőben különböző detektor–forrás távolságok esetén (görbe paraméter)

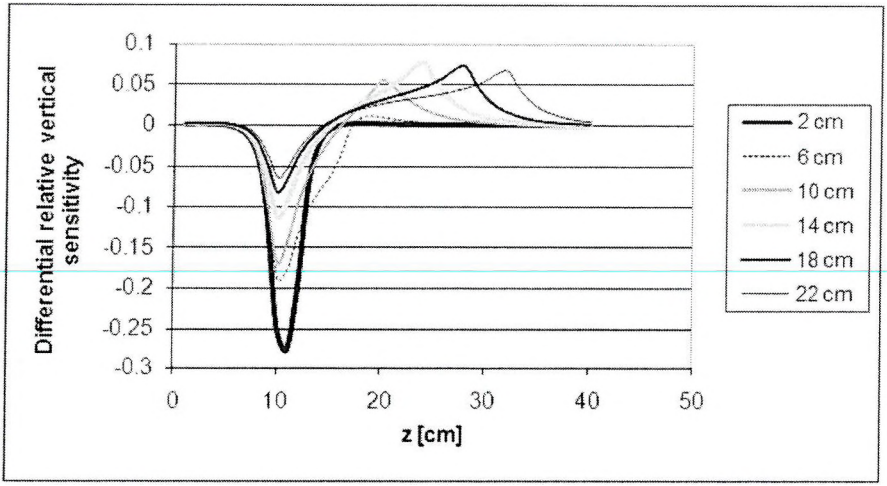

Fig. 7. Differential relative vertical sensitivity functions in 20% porosity sandstone (embedded thin layer effect). The source is located at z = 10 cm. The curve parameter is the detector–source distance

7. ábra. Differenciális relatív függőleges érzékenységi függvények 20% porozitású homokkőben (beágyazódott vékony réteg hatása). A forrás z = 10 cm-nél helyezkedik el. A görbe paramétere a detektor–forrás távolság

$$\Sigma_i(\mathbf{r}) = \frac{\int_{E_{1,i}}^{E_{2,i}} \Sigma(E,\mathbf{r})\,\varphi(E,\mathbf{r})\,\mathrm{d}E}{\int_{E_{1,i}}^{E_{2,i}} \varphi(E,\mathbf{r})\,\mathrm{d}E} \tag{21}$$

Below 5% porosity, not only does the flux anisotropy cause a problem close to the source, but so does the strong variation of neutron spectra. In this case the Maxwell–Boltzman type distribution at thermal energies is not formed perfectly, so the thermal group coefficient should be calculated using different weighting functions.

In Figs. 8a and b, the spectrum variation is displayed as a function of distance from the neutron source. The Maxwell–Boltzman type spectra can easily be identified in lower energy.

In the Monte Carlo calculation the sonde model was also more realistic, as can be seen in *Fig. 9.*

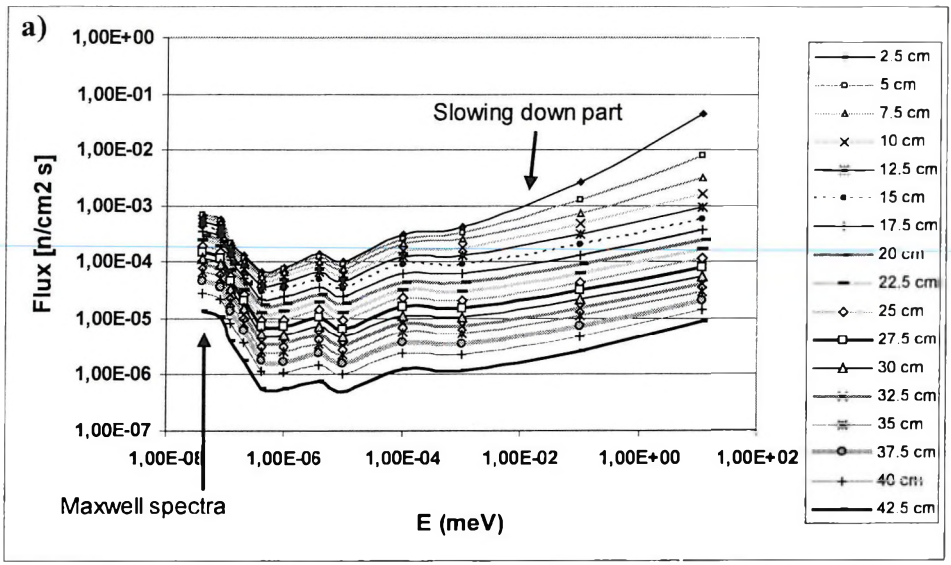

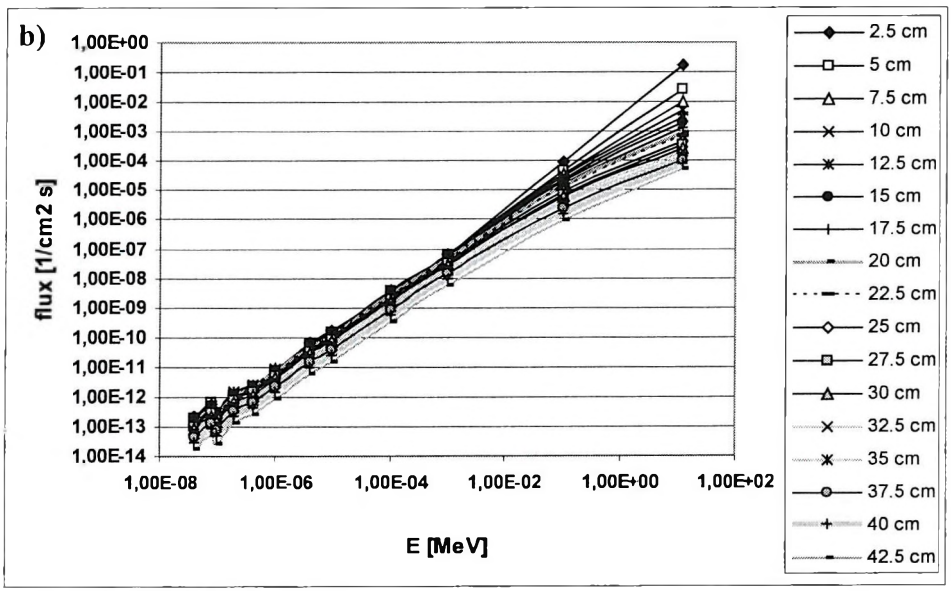

Fig. 8. Spectral variation of neutron field in 20% (**a**) and in 0% (**b**) porosity sandstone, at different distances from point source (Am–Be) by Monte Carlo calculation

8. ábra. A neutron tér spektrális változása 20% (**a**) és 0% (**b**) porozitású homokkőnél a pontforrástól (Am–Be) különböző távolságokban Monte-Carlo-számítással

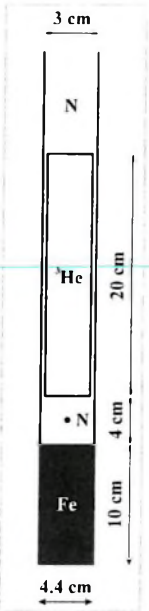

Fig. 9. Penetration neutron sonde model applied in the Monte Carlo calculation
9. ábra. A Monte-Carlo-számításnál alkalmazott penetrációs neutron szonda modell

5. Radial sensitivity

During spectral studying of the neutron field, the finite model effect was also investigated to determine the rock cylinder measure, which is a good approximation for the infinite medium.

This series of Monte Carlo calculations allows one to derive the radial sensitivity (geometric factor) function (*Fig. 10*). In this study the embedding rock cylinder is increased step by step, and the thermal flux in the detector volume is calculated and compared with the reference case.

The flux can be derived by integrating the thermal neutron path in the detector volume, which is normalized with the neutron number emitted from the source in the simulation process.

The results of Monte Carlo and two group diffusion methods are compared in *Fig. 11*. It should be noted that the difference between the two types of results mainly originates from the model difference.

If the model for Monte Carlo calculation is a series of thin perturbed cylindrical shells (*Fig. 12*), the results are those displayed in *Fig. 13*.

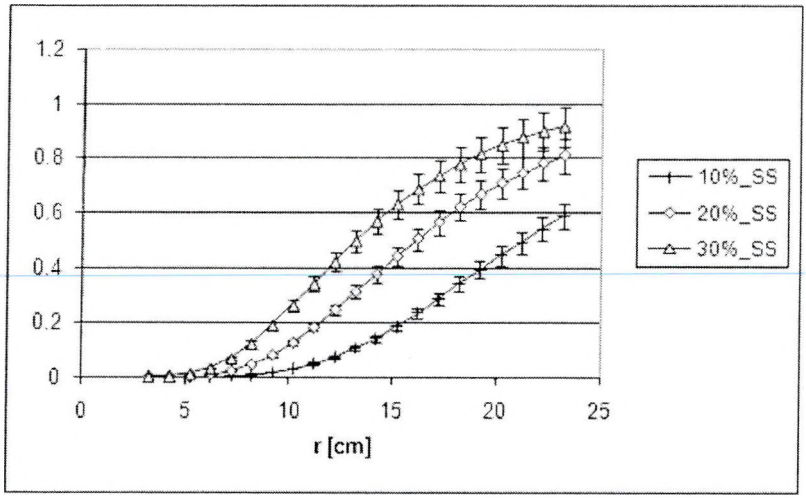

Fig. 10. Radial sensitivity ('geometric factor') curves of neutron sonde in different porosity sandstone (SS). The curves are derived by Monte Carlo calculation using a series of finite cylinders as rock models. The parameter of curves is the porosity of sandstone

10. ábra. A neutron szonda sugárirányú érzékenységi (geometriai tényező) görbéi különböző porozitású homokkövekben. A görbéket a Monte-Carlo-módszerrel vezettük le, kőzetmodellként véges hengerek sorozatát használva. A görbék paramétere a homokkő porozitása

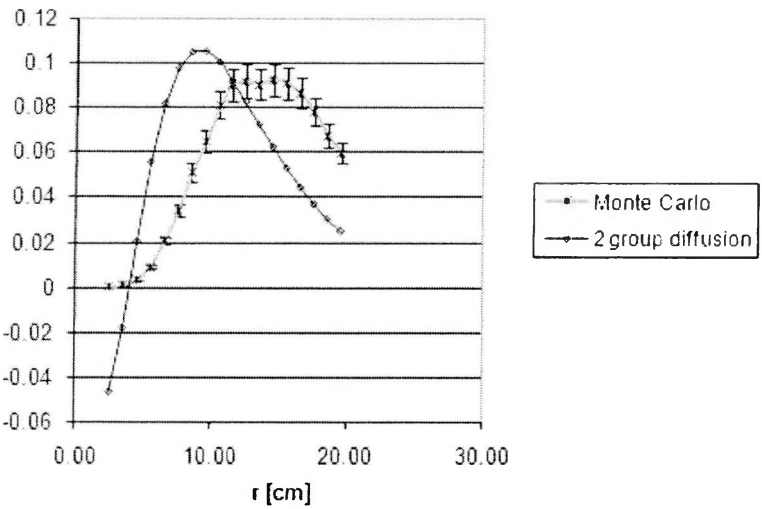

Fig. 11. Comparison of differential radial sensitivity (differential geometric factor) curves originating from the Monte Carlo and the two group diffusion method

11. ábra. A Monte-Carlo és a kétcsoportos diffuziós módszerből származó differenciális sugárirányú érzékenységi (differenciális geometriai tényező) görbék összehasonlítása

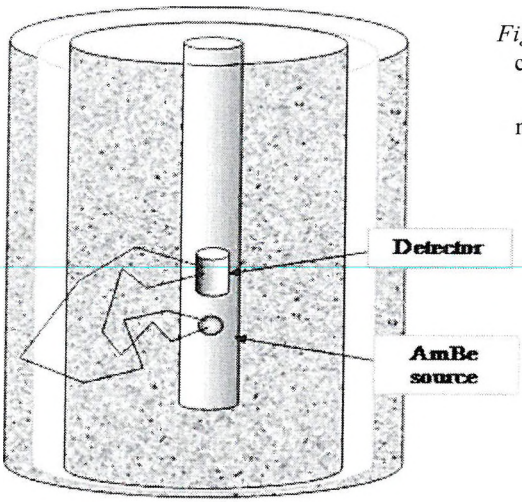

Fig.12. The second model of Monte Carlo calculation: perturbed cylindrical shell

12. ábra. A Monte-Carlo-számítás második modellje: perturbált hengeres héjszerkezet

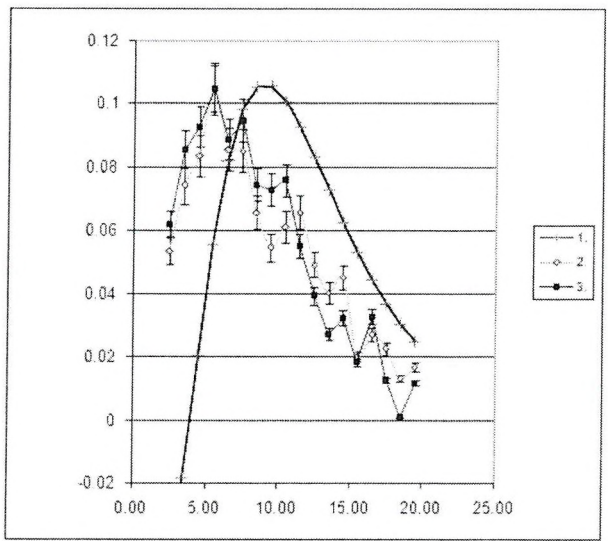

Fig.13. Relative differential radial sensitivity — comparison of results of Monte Carlo and two group diffusion method for cylindrical shell type perturbation in 20% porosity sandstone. *Curve 1*: results of two group diffusion method; *Curve 2*: results of Monte Carlo calculation when the density of perturbed cylindrical shell was 0 g/cm^3; *Curve 3*: results of Monte Carlo calculation when the porosity of perturbed cylindrical shell was 22%

13. ábra. Relatív differenciális sugárirányú érzékenység — a Monte-Carlo és a kétcsoportos diffúziós módszer eredményeinek összehasonlítása hengeres héjszerkezetű perturbációra 20% porozitású homokkőben. *1. görbe*: a kétcsoportos diffúziós módszer eredményei, *2. görbe*: a Monte-Carlo-számítások eredményei arra az esetre, amikor a perturbált hengeres héjszerkezet sűrűsége 0 g/cm^3 volt. *3. görbe*: a Monte-Carlo-számítás eredményei, arra az esetre, amikor a perturbált hengeres héjszerkezet porozitása 22% volt

From the results regarding the radial sensitivity it can be seen that the research depth of the penetration neutron sonde is slightly smaller than is generally shown in the literature [TITTMAN 1986]. Even though a research depth of 30–40 cm is generally given, from the calculations just 20 cm is the characteristic value. The most important radial region (where the radial sensitivity curve reaches its maximum) is around 10–15 cm depending on the rock type.

6. Vertical inhomogeneity

The effect of vertical inhomogeneities for penetration neuron logs was also studied by Monte Carlo calculation.

In *Fig. 14* the bed boundary effect is demonstrated, and in *Fig. 15* the thin layer effect can be seen. The example displayed in Fig. 15 also confirms that the maximum and dominant part of the vertical resolution curve

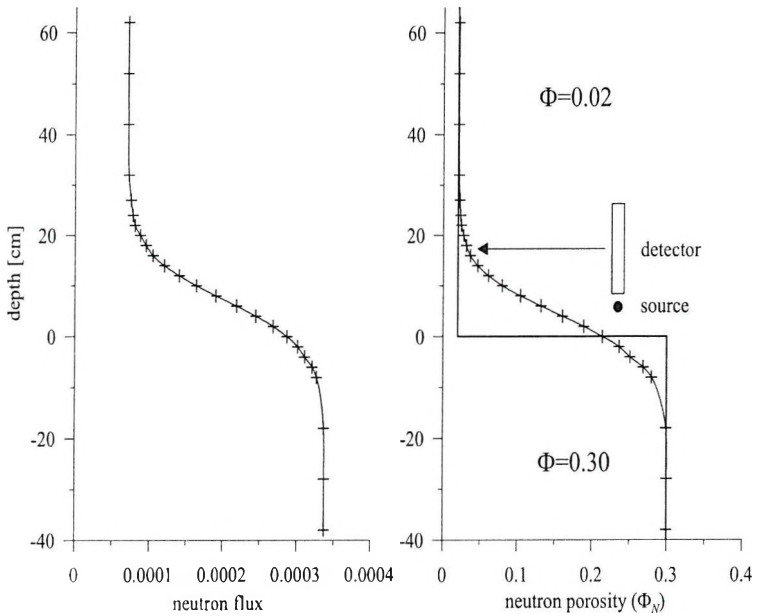

Fig.14. Bed boundary effect calculated by Monte Carlo method (transition from 30% porosity sandstone to 2% porosity)

14. ábra. Monte-Carlo-módszerrel számított réteghatár hatás (átmenet a 30%-os porozitástól a 2%-os porozitásig)

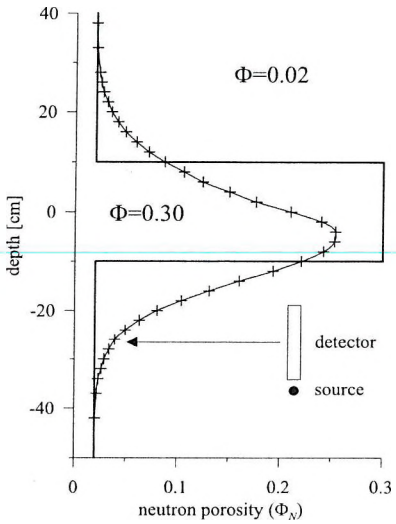

Fig. 15. Thin layer effect calculated by Monte Carlo method.
15. ábra. Vékony réteg hatás Monte-Carlo-módszerrel számítva

is positioned at the source, as can be seen in Fig. 7. This effect explains the shift of maximum in the simulated porosity curve (as can be predicted from Fig. 15).

7. Examination of some sonde parameters

In this section the Monte Carlo calculation capacity is demonstrated in the area of sonde design.

In *Fig. 16* the effect of detector volume can be followed comparing the porosity–thermal neutron flux calibration curves. *Figure 17* shows the sonde wall thickness effect with the thermal flux–porosity curves. In the second case the sonde wall thickness is incremented by 1 mm. Finally the effect of neutron source–detector distance is examined by the Monte Carlo method. The porosity–thermal flux calibration curves are calculated at different source–detector distances (*Fig. 18*). On the basis of the curves, the minimal source–detector distance is recommended to achieve the best sensitivity profile. The direct radiation, which is moderated in the sonde body, has a negligible effect.

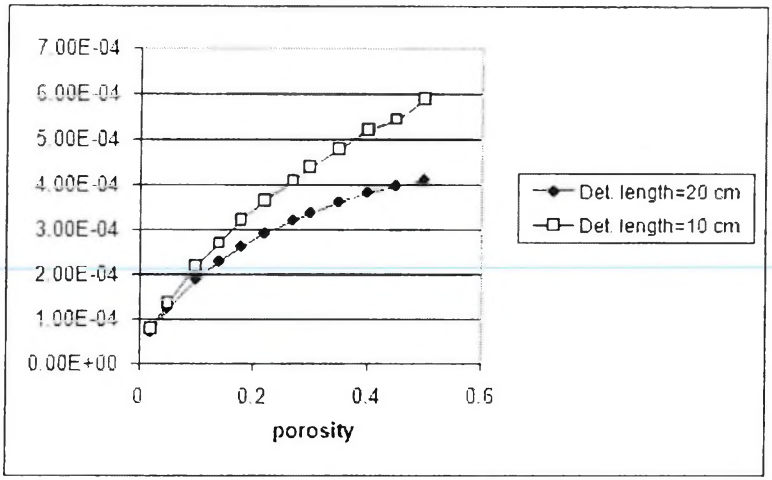

Fig. 16. Count rates (CPS) of detectors as a function of porosity. The parameter of calibration curves is the detector length

16. ábra. A detektorok számlálási sebessége (CPS) a porozitás függvényében. A kalibrációs görbék paramétere a detektor hossza

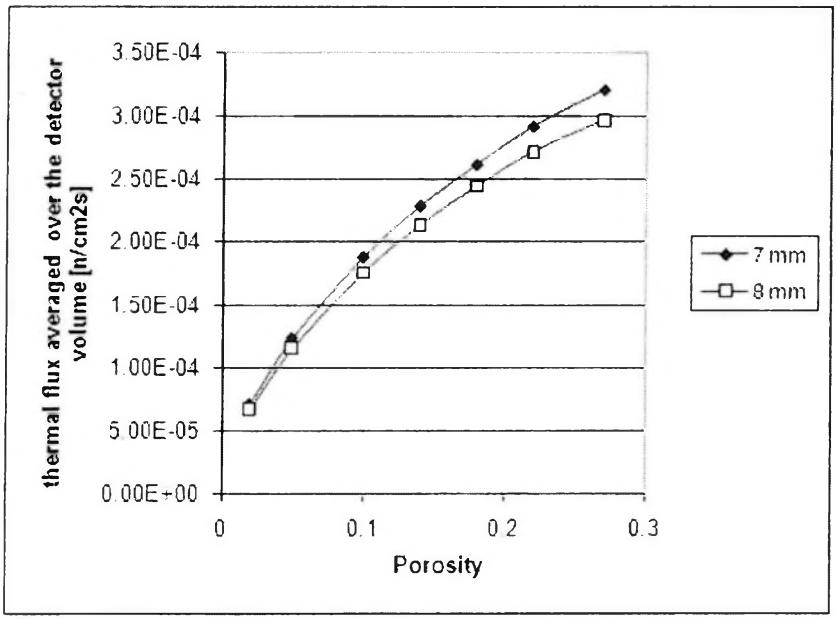

Fig. 17. Effect of sonde wall thickness (curve parameter) on the calibration curves. The detector length was 20 cm, the embedding rock was sandstone

17. ábra. A szondafal vastagságának hatása (görbeparaméter) a kalibrációs görbére. A detektor hossza 20 cm, a beágyazó kőzet homokkő volt

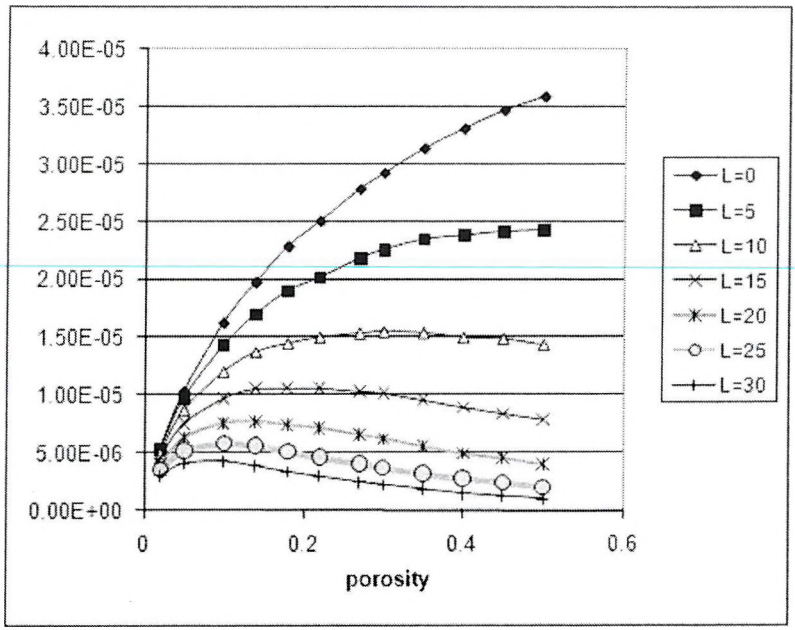

Fig. 18. Calibration curves — thermal flux vs. porosity — for different source–detector distances. The detector length was 20 cm

18. ábra. Kalibrációs görbék — hőfluxus és porozitás — különböző forrás–detektor távolságokra. A detektor hossza 20 cm volt

8. Conclusion

The behaviour of a penetration neutron sonde was investigated by two methods. Although the two methods give different results because of the different approximation, it can be concluded that the investigation depth was smaller than can be found in the literature in the case of conventional neutron tools. For sandstone the characteristic values are between 5 and 15 cm. In some books, e.g. TITTMAN [1986] the geometric factor — which characterizes the sonde investigation depth — is derived from the decrement of thermal flux function. From our results it can be seen that the different approximation of detector importance function is a better function for this purpose.

From the results regarding the vertical resolution it becomes clear that the dominant part of the measured rock region is located at the source in the medium and high porosity rock.

The spectral changes of the neutron field are also investigated to demonstrate the difficulties of group constant calculations especially for low porosity rocks.

Finally the important calibration curves are given taking into account the effect of some important sonde parameters. The most important conclusion from these curves is that the smallest detector–source distance is recommended. The small distance has almost no effect on the investigation depth.

Acknowledgement

This research was supported by the Hungarian Scientific Research Fund (OTKA) in the framework of project No: TO43748

REFERENCES

ARFKEN G. B., WEBER H. J. 1995: Mathematical methods for physicists. Academic Press, Boston

ENDFVI Library: Evaluated Nuclear Data File, 2 November, 2001. Cross Section Evaluation Working Group (SCEWG) U.S., Canada

KISS D., QUITTNER P. (eds.) 1971: Neutronphysics (in Hungarian). Akadémiai Kiadó, Budapest

KNOLL G. F. 1989: Radiation detection and measurement. John Wiley & Sons, New York, 816 p.

STACEY W. M. 2001: Nuclear Reactor Physics. Wiley-interscience, New York 706 p.

SZATMÁRY Z. 2000: Introduction to Reactor Physics (in Hungarian). Akadémiai Kiadó, Budapest 408 p.

TITTMAN J. 1986: Geophysical Well Logging. Academic Press, London, 175 p.

A penetrációs neutron szonda viselkedésének modellezése és vizsgálata különböző feltételek esetén Monte-Carlo-módszerrel és diffúziós közelítéssel

BALÁZS László

A neutron szondák mérésének modellezéséhez a neutronokra vonatkozó transzport egyenletet kell megoldani az alkalmazott elméleti mérési modellek feltételei mellett. Jelen cikkben a szonda viselkedésének tanulmányozásához egy sor tematikus, változó paraméterű modellre oldottuk meg a direkt feladatot pontszerű Am–Be neutronforrás terére vonatkozóan, melyek segítségével vizsgáltuk a szonda viselkedését és térbeli érzékenységét (pl. kutatási mélység és vertikális felbontás).

Meghatároztuk a penetrációs szonda radiális érzékenységét reprezentáló geometriai faktor függvényeket, illetve a vertikális felbontásra vonatkozó érzékenységi görbéket. Előállítottuk továbbá a szonda fontosabb kalibrációs görbéit is.

A számításokat Monte-Carlo-módszerrel és kétcsoportos diffúziós közelítéssel is elvégeztük.

ABOUT THE AUTHOR

László Balázs received his M.Sc. in geophysics from the Eötvös Loránd University in 1985, then he joined the Geophysics Department of the Hungarian Hydrocarbon Research Institute where he dealt with the theoretical modelling of different types of geophysical sondes. He then became a lecturer in the Institute of Nuclear Techniques of the Budapest University of Technology and Economics, and currently works in the Department of Geophysics of Eötvös Loránd University, Budapest.

GEOPHYSICAL TRANSACTIONS 2008
Vol. 45. No. 3. pp. 157– 177

Parametric interpolation of seismic velocity field

Greg DETZKY*

Structural geological interpretation in reflection seismology is traditionally carried out by using sections presented in the dimension of reflection time. In order that the structural geological information resulting from operations performed in this dimension can be used together with other detailed information it is necessary to have appropriate transformation between reflection time versus depth space and vice versa. This step is a typical and indispensable operation of geoscience projects including seismic interpretation. There are many traditional calculation methods for this purpose. Most of them involve utilizing some kind of direct interpolation of irregularly distributed numerical samples from 3-D velocity space. The present paper proposes a new numeric method: the parametric interpolation for the same purpose. This can reduce the solution of the original 3-D problem to a 1-D approximation followed by a 2-D interpolation thereby enabling one to realize the same task by more simple software tools. Following on from the principle of the given procedure, calculation remains reliable even in sparsely sampled areas. An additional benefit of the proposed procedure is the seamless transferability of the usual anisotropic character in the gradient of velocity fields of sedimentary basins without having a specific numeric solver dedicated to handle this particular feature. Analysis focused on the interdependences of function parameters used especially to approximate velocity field data from the real test territory revealed unexpected regression dependences of these parameters.

Keywords: seismics, numeric method, sedimentary basin, stacking velocity

1. Motivation for 3-D interpolation of seismic velocity fields

In reflection seismology the interpretation is traditionally carried out on time sections. To accomplish the task adequately one must have a good structural and historical view of the given objects. This demands the combined use of information derived from tectonic and stratigraphic elements on the sections both in reflection time space and well data given in depth space.

To enable the combination of the stratigraphic data of wells given in depth, and objects from reflection seismic sections available in TWT (vertical dimensions measured in two-way time) the depth of data from wells

* Eötvös Loránd Geophysical Institute 1145 Budapest, Kolumbusz u. 17-23. Hungary
Manuscript received (revised version): 2. October, 2006

should be transformed into reflection time or, sometimes vice versa, its seismic counterparts to depth. In better cases the sonic or VSP data are available along wells enabling direct and precise definition of reflection time/depth dependence. In the case of projects having a lot of usable well data but lacking well-log velocity information, it is preferable to obtain interpolated velocity data as precisely as possible at well sites from other sources of velocity information. This provides a means for transforming stratigraphic data of wells from depth to reflection time.

Structural interpretation performed on data from 2-D seismic networks and well data usually results in an intermediate structural model in the reflection time dimension. Although integrating structural geological data obtained in such a way together with other geological datasets, e.g. depth-converted tectonic maps, were originally compiled in reflection times, they might well be utilized in other branches of application geology such as preparation for oil exploitation, working strictly in the depth dimension. The reliable and consistent approximation of velocity fields at any point of a given 3-D space is a precondition for all the above mentioned issues.

2. Parametric interpolation

2.1. Parametric interpolation process of seismic velocity field

Datasets representing the seismic velocity field — depending on how they were created — could differ substantially in resolution and cost. In the territories investigated by 2-D seismic projects the most diverse sources of data usable for 3-D velocity field representation are the NMO or DMO stacking velocity data sequences. The stacking velocity data are always results of the conventional velocity analysis phase of the processing. These items of data are given at ascendant TWT values related to a particular surface reference point. Compared to seismic velocities determined by other direct methods, the stacking velocities have medium accuracy and resolution but provide quasi-homogeneously distributed velocity information usually covering the whole of a studied area and are composed of many data samples. Therefore these datasets could form a good input for interpolation of the velocity field.

The parametric interpolation procedure replaces direct 3-D interpolation by a 1-D approximation and by a 2-D interpolation performed after-

wards. During the first stage of the 1-D approximation procedure, unique parameter sets are calculated for an appropriately chosen analytic function resulting in optimal fitting to the sequences of the stacking velocity values. These are irregularly spaced along the reflection time at the different surface locations of the stacking velocity analysis points. There are many simple license-free software solutions available on the Internet or software in daily practical use in other tasks of geophysics which can be used for this type of calculation.

A good candidate for analytical 1-D approximation of seismic velocity fields is a function involving finite asymptotic limits in $\pm\infty$ and being able to differentiate at any point. The algebraic polynomials, for example, are not among the best choices because they do not fulfil the first requirement. They tend to produce values that are extremely different from base data ranges even in the close vicinity of the interpolation intervals. It is worth avoiding this type of function for the sake of the stability in analytical approximations of seismic velocity fields.

In the second stage of parametric interpolation the unique parameter sets of the approximation function instances related to given surface points of the area must be interpolated horizontally in 2-D. Grid generation functions of conventional isoline mapping software are usually suitable for this. As a result of these computations a 'function space' of the local vertical approximation functions of the 3-D velocity space is created. This planar function space is presented in surface parallel grids of the particular approximation parameters. This makes possible a consistent estimation of the stacking velocities at practically any 3-D point by an approximation in depth with parameters interpolated onto the given surface location.

In the third stage of the whole procedure, a parametrically interpolated velocity field could be used for practical transformation purposes by numeric integration of the approximation function instances at the location points of the object (i.e. layer depths in bore holes, etc).

2.2. Mathematical introduction of an approximation function suitable for parametric interpolation of seismic velocity data

Conventional seismic velocity analysis operations of reflection processing flow produce stacking velocity sequences close to the $V = V_{rms}(T)$ velocities along ascendant reflection time values (T) relating to the surface reference locations of velocity analyses. Replacement of NMO stacking

velocities in the case of nearly horizontal layers, or DMO stacking velocities in the case of dipping layers with V_{rms} velocities yields a satisfying approximation in exploration with average requirements [VEEKEN et al. 2005].

Based on practical experience, velocity function forms occurring in the Pannonian Basin reaching only average oil exploration depths can satisfactorily be approximated by using a category of the function illustrated in *Fig. 1*; the function forms were chosen by the character of the actual curve shapes and could generally be defined by

$$V = V_0 + a\frac{bt - \tau}{\sqrt{(bt - \tau)^2 + 1}} \tag{1}$$

This is a form of the derivative of a hyperbole with a vertical axis, extended with appropriate transformation parameters. The function should correspond with such selection criteria as asymptotic co-domain, overall derivativity and simple parameter settings (for explanation, see *Section 2.1.*)

Unique parameters of the given approximation function could be termed by such expressive physical meanings as inflection velocity V_0 — the velocity at the inflection point of the function; velocity range a — the difference between the asymptotic and the inflection velocity; inflection gradient b — the differential coefficient at the inflection point; inflection time τ/b — the time value of the function at the inflection point which is measured in terms of reflection time. At this τ/b time the gradient of V_{rms}

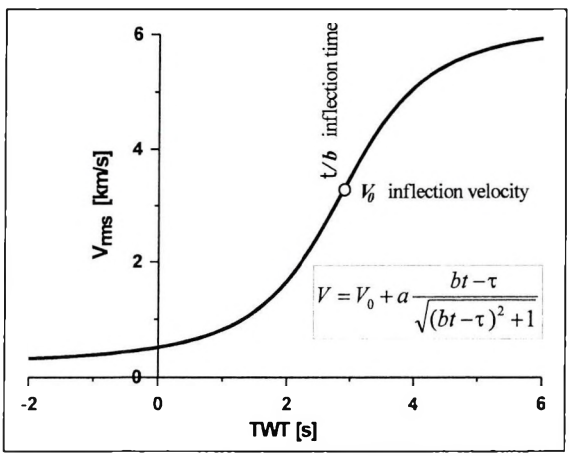

Fig. 1. Function category suitable for approximation of V_{rms} velocity functions occurring in the Pannonian Basin. Parameters of this curve: V_0=3.2 km/s; a=3 km/s; b=0.7; τ=2 s (for details, see text)

1. ábra. A Pannon-medencében előforduló V_{rms} sebességfüggvények közelítésére alkalmas függvénytípus. A megjelenített görbe paraméterei: V_0=3.2 km/s; a=3 km/s; b=0.7; τ=2 s (további információ a szövegben)

velocity reaches the greatest value *ab* and the velocity itself is equal to V_0.

Many algorithms exist as a means of obtaining the numerical values of the parameters defining a particular best fitting approximation function of a given sort. A well-tested algorithm implemented by Ernő Prácser in ELGI based on partial separation of Jacobi matrices at singular values has proved its effectiveness and reliability in the practical data processing tasks of many different branches of applied geophysics [SHARMA et al. 2005]. In the current case the algorithm provides numerical parameters for chosen velocity approximation functions with unbroken stability, reaching theoretical optima at a predefined accuracy with fast convergence (less than 30 iterations).

Let a sort of function generally defined by eq. (1) be used to approximate the input V_{rms} data sequences. Substituting this into the differential counterpart (eq. (3)) of the well known [MESKÓ 1977] integral equation (2) describing the interdependence of the interval (v) and the RMS (V) velocities in the continuously variable medium

$$TV^2(T) = \int_0^T v^2(t)\mathrm{d}t \tag{2}$$

$$[tV^2(t)]'_t = V^2 + 2tVV' = v^2(t) \tag{3}$$

a more complex — but from the viewpoint of numeric computation still sufficiently simple and useful eq. (7) — could be obtained. (The sign ' is for the first derivative.)

Rearranging eq. (1)

$$\frac{V - V_0}{a(bt-\tau)} = \frac{1}{\sqrt{(bt-\tau)^2+1}} \tag{4}$$

and by derivation of eq. (1)

$$V'_t = a\left[\frac{b\sqrt{(bt-\tau)^2+1}}{(bt-\tau)^2+1} - \frac{1}{(bt-\tau)^2+1}\left((bt-\tau)\frac{1}{2}\frac{2b(bt-\tau)}{\sqrt{(bt-\tau)^2+1}}\right)\right] =$$

$$= ab\left[\frac{1}{\sqrt{(bt-\tau)^2+1}} - (bt-\tau)\frac{1}{(bt-\tau)^2+1}\frac{(bt-\tau)}{\sqrt{(bt-\tau)^2+1}}\right] \tag{5}$$

Then, by appropriate substitution from eq. (4) to eq. (5),

$$V_t' = ab\left[\frac{V-V_0}{a(bt-\tau)} - (bt-\tau)\frac{(V-V_0)^2}{a^2(bt-\tau)^2}\frac{(V-V_0)}{a}\right] = \tag{6}$$

$$= \frac{b}{(bt-\tau)}\left[(V-V_0) - \frac{1}{a^2}(V-V_0)^3\right]$$

and, finally, by substitution from (6) to (3)

$$v^2 = V^2 + 2V\frac{bt}{(bt-\tau)}\left[(V-V_0) - \frac{1}{a^2}(V-V_0)^3\right] \tag{7}$$

The formula given in (7) is an analytical equation defining vertical 1-D approximation of the $v = v_{int}(t)$ interval velocity field to be referred to at any surface point by 2-D interpolation of its parameters.

Numerical integration of the square root of eq. (7) using the following

$$v_a(T) = \frac{1}{T}\int_0^T v(t)\mathrm{d}t \tag{8}$$

formula (8) of the medium with continuously changing velocity [MESKÓ 1977] provides the final result at any predefined accuracy. This is the estimation of the 3-D distribution of v_a average velocity needed to transform the data given in depth into reflection time and vice versa.

The described computation method actually starting from irregularly sampled RMS velocity data (V_{rms}) in the investigated 3-D space, produced by seismic velocity analyses results in the numerical definition of the v_a average velocity field, seamlessly interpolable into any 3-D point or grid of the covered space. Numerical integration needed in the last stage of the procedure does not degrade the effects of the most important practical advantages of parametric interpolation, such as the transparency against velocity gradient anisotropy (*see Section 2.4*), and the reduction of the problem to lower numbers of dimensions.

As a summary it can be stated that data given in depth (i.e. well-stratigraphy data) related to any surface location of the area can be converted into reflection time (needed prior to the beginning of any seismic interpretation work), by utilizing parameters of approximation eq. (1) provided by the

parametric interpolation. At the same time structural geological elements resulting in reflection time by seismic interpretation could vice versa be seamlessly converted to depth.

2.3. Testing of the suggested approximation function by real velocity data

A batch mode drawing program provides a visual checking tool. This drawing program was developed especially for the task of graphic quality control of the approximation using the approximation function suggested in *Section 2.2* by joint plotting of the original numerical velocity samples and approximation curves.

The analytical equation used for 1-D approximation of velocity data sequences on the test area (which corresponds with the 150x50 km territory of the Szolnok Flysch formation) was defined by graphical checking of about 1200 real velocity function datasets originating from sedimentary basins of Hungary, without limiting this checking to those 486 sets located in the test polygon.

Taking into account the overall 'morphological' characteristics of the source function set, a conclusion could be drawn about the good fitting of the approximation by the appropriate parametric scaling of the basic function form shown in *Fig. 2.* The occasional poor adaptivity of the applied approximation algorithm or any given function type has less effect on the error level of the approximation fitting of the real stacking velocity data than sampling reliability variations of velocity analysis in the preceding seismic processing. Judging from practical experience on such errors, values which make further usage of the approximated data impossible rarely occur and even those are mostly caused by errors in the input datasets, not by stratigraphic extremities. None the less badly approximated single curves with parameters greatly differing from the neighbouring curves could easily be selected by preventive graphical checking (Fig. 2.) and then excluded from the general interpolation of the regional velocity field. The lack of approximation curves with irreal data among the test samples, even for short or 'noisy' input datasets, indicates the strong stability of the chosen type of approximation function and algorithm. Consequently, seismic time–depth conversion on this basis can also be considered relatively error-proof.

Isoline mapping of the RMS difference between original V_{rms} velocities and approximated values is probably the most convenient way of qual-

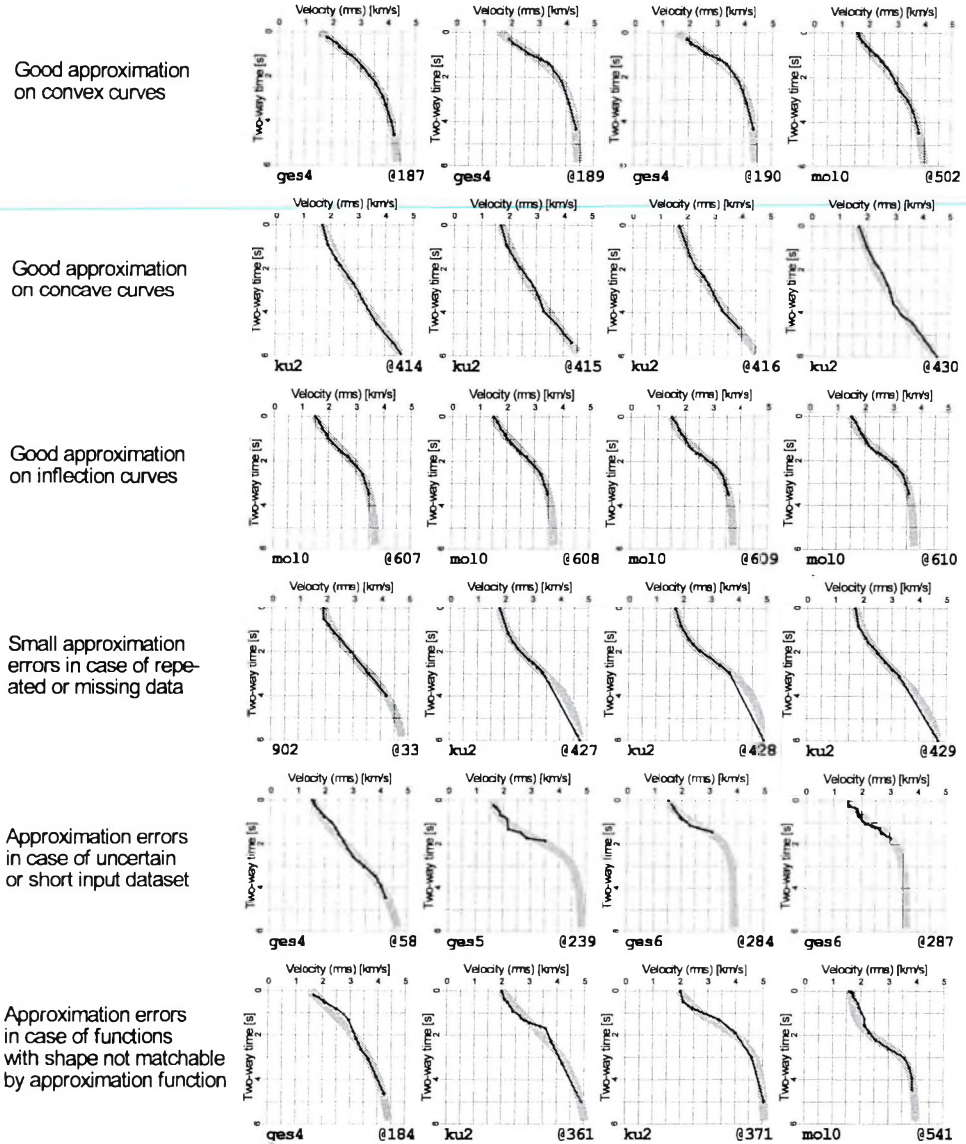

Fig. 2. Typical V_{rms} function curves and quality of analytical approximation

2. ábra. Tipikus V_{rms} függvénygörbék és az analitikus közelítés minősége

ity and reliability assessment of the velocity field interpolated by the parametric method. Taking into account the data of the test area (*Fig. 3*) we can see that the RMS error of approximation is below 30 m/s even in the worst places. This means an error level of less than 1% in relation to a ususal 3000 m/s seismic velocity in most parts of the area. Therefore in this particular case of the original velocity data of the test area and the chosen approximation function, the approximation itself can be considered of high quality which therefore encourages the widening of application to other territories too.

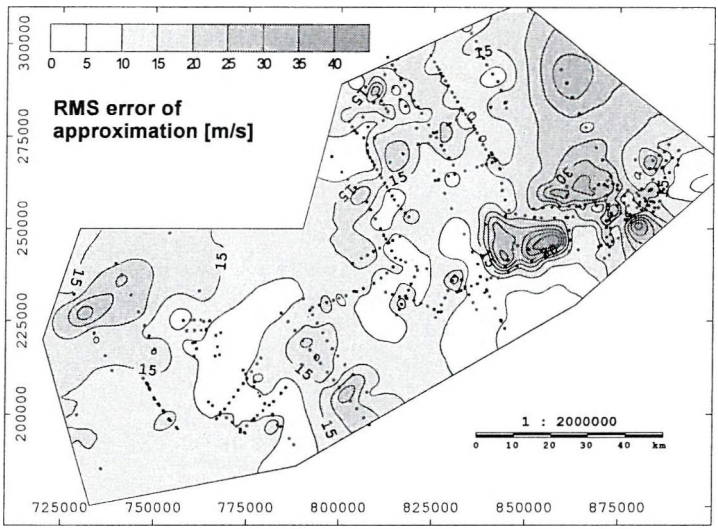

Fig. 3. RMS difference of approximation function values and V_{rms} data on the test area given in m/s

3. ábra. A teszterület V_{rms} adatai és az approximációs függvények átlagnégyzetes eltérése m/s-ban

2.4. Comparison test of direct and parametric interpolation for an anisotropic gradient in the velocity field

Statistically inhomogeneous direction characteristics of variation in the quantity to be interpolated (usually represented by an ellipsoid) could be transferred to the interpolated result by the direction characteristics of the interpolation weights, properly fitted to the characteristics of the original field itself. In most cases of 2-D interpolation software these character-

istics could be defined as constant as they remained unchanged during all of the given interpolation sessions. The most sophisticated procedures are capable of adaptively following the variation in space of the original dataset's characteristics but they are only built into the more expensive software categories. In cases of 3-D interpolation of seismic velocity fields with higher quality requirements, automatic adaptation to the horizontally gently changing anisotropy of the velocity field is favourable. This capability is an inherent feature of the parametric interpolation procedure. One of the most appropriate ways of estimating the magnitude of influence caused by the above-mentioned effect on the results is model calculation.

Assuming such a model in which the vertical change of the seismic velocity field exactly corresponds with the approximation function introduced in *Section 2.2* and the parameter changing of this function in the horizontal direction is linear as in the case of the sample functions in *Fig. 4/a* correlating with basement depth as an independent geological parameter, a model field could be obtained similar to that in the section of *Fig. 4/c.* Sectionwise linear parameter dependence of the model function to be studied is given in *Table I* at rounded km distances. This type of velocity distribution is similar to many real cases.

Giving a simple explanation, one could say that if minimum/maximum zones of the velocity field are elongated parallel to the axes of the zonation in geological features, then longer effective interpolation distances should be considered by that direction. Mathematically this means that the maximum axes direction of the interpolation characteristics should correspond with the direction marked by cross-correlation maxima calculated on samples of the original field's derivative.

(The eccentricity of the characteristics may be optimized by variance analysis of the original data.) Dipping directions in reflection time given by cross-correlation maxima of the derived model field at a distance of 5 km distance and at other marked sampling axes are linearly related to the basement depth (*Fig. 4/b.*).

Fig. 4. Comparison of interpolations by parametric methods and local polynomial fitting for an anisotropic field. **a** – input approximation functions, **b** – cross-correlation functions of the derivative at 5 km and at the other marked section points, **c** – V_{rms} model velocity field, **d** – velocity field resulting from local polynomial fitting after exclusion of the 'middle' input function (at 3 km), **e** – residual difference of the original and interpolated fields.)

⇒

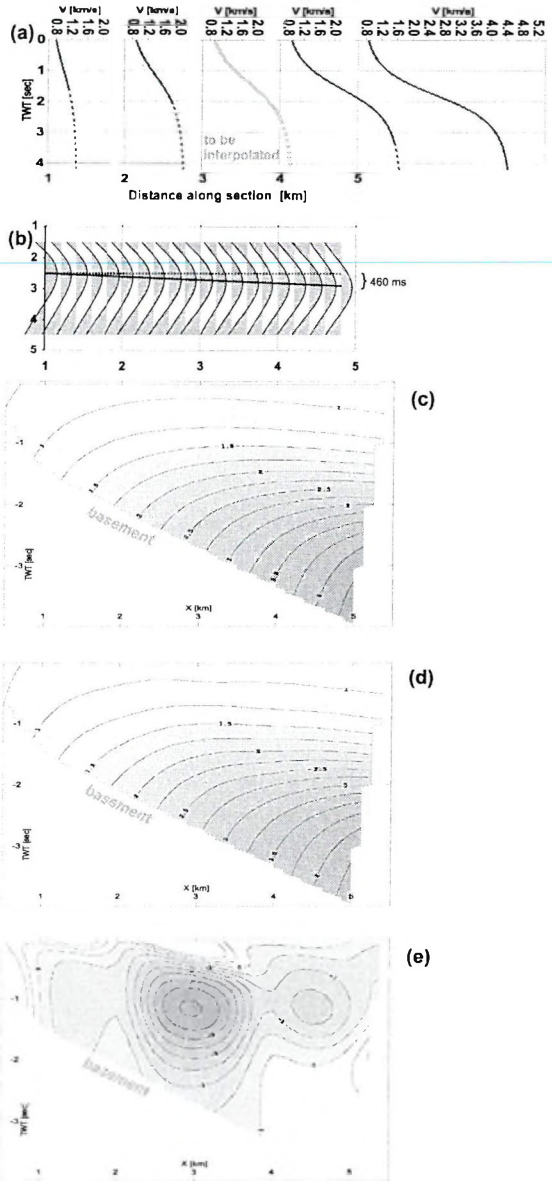

4. ábra. A parametrikus módszerrel és lokális polinómillesztéssel végzett interpoláció összehasonlítása anizotróp tér esetén. (**a** – kiinduló approximációs függvények, **b** – az 5 km-es távolság és a többi jelölt szelvénypont deriváltfüggvényeire számított keresztkorrálációs függvények, **c** – V_{rms} sebességtér modell, **d** – a középső [3 km] pont modellfüggvényének kizárása után, lokális polinomiális illesztéssel kapott sebességtér, **e** – az eredeti és interpolált sebességterek reziduális különbsége.)

parameter	***x*/1000 [m] ->**	**1**	2	**3**	**4**	5
Inflection velocity	V_x [km/s]	1	1.4	**1.8**	2.2	2.6
velocity range	*a* [km/s]	0.4	0.8	**1.2**	1.6	2
inflection gradient	*b*	0.6	0.7	**0.8**	0.9	1.0
parametric time	τ [s]	0.6	0.84	**1.12**	1.44	1.8
inflection time	τ/*b* [s]	1	1.2	**1.4**	1.6	1.8

Table I. Model velocity field for checking the effect of anisotropy given by parameters of its approximation function at round km distances

I. táblázat. Az egész km értékű szelvénypontokban, a paraméterei által megadott sebességtér modell az anizotrópia hatásának ellenőrzésére

2-D linear model fields created for testing simplicity in the way described above have a useful practical property: this property being the general equality of their original values and estimated values to be calculated by parametric interpolation of approximation functions related to any pair of surface points.

Any type of interpolation used for 'patching' in a blank space, made by partially abandoning the original data, could be considered comparable to parametric interpolation in terms of quality if it provides values in the blank spaces with just a tolerable difference from the original data. The isolined section shown in *Fig. 4/d* results from local polynomial fitting interpolation of the model field when the input dataset is created by sampling (with sufficient vertical density) of the four velocity functions shown by the curves in Fig. 4/a and given by the parameters in Table I, neglecting the middle function at 3 km (marked in bold).

Amongst the interpolation algorithms ready for immediate use it was the 'local polynomial fitting' with anisotropy characteristics adjusted to the maximum correlation direction which provided the most acceptable results.

Even though the difference in the shapes of the isolines from the original (Fig. 4/c) and interpolated (Fig. 4/d) data is hardly noticeable by the naked eye, the residual difference of these two datasets reaches 4 % as can be seen in the section of *Fig. 4/e*. This difference is many times more than 1% (or less) of the error shown in Fig. 3, experienced between the real data and the functions introduced for approximation.

It may be assumed that the velocity field interpolation with constant anisotropy characteristics covering both opposite direction dipping banks (i.e locations with different anisotropy) of a sedimentary basin will probably produce higher average error values than those obtained in the current model. In contrast, the accuracy of the parametric interpolation — by virtue of its principles — is basically independent of the variation of the anisotropy directions in the velocity field.

3. Regression dependence between parameters of the applied approximation function

The possible existence and character of the regression dependence between parameters related to the approximation function used on a given region could most adequately be explored by crossplots. The ability to reveal the existence of the various regression dependences between approximation parameters of the test territory is an unexpected extra result of those studies utilizing parametric velocity field interpolation. There are dependences between parameters of analytic approximation functions of the V_{rms} velocity functions shown by *Fig. 5*. These denote at the same time the interconnection of properties (see *Section 2.2*) bound to the presumed physical parameters.

Taking into consideration the crossplots in Fig. 5, the character of the apparent dependence between inflection gradient and velocity range is hyperbolic, between inflection gradient and relative inflection time it is linear, and between inflection velocity and absolute inflection time it is exponential. Consequently, in the case of practical velocity functions, prescribing any of the four parameters of the interpolation function that is used results in specific probabilistic values for the remaining three.

Higher order parameters of the specific function parameter dependences might be typical of the test area or global characteristic quantities of the usual geological media in sedimentary basins. Clarification of the real origin of these dependences is a subject for further research.

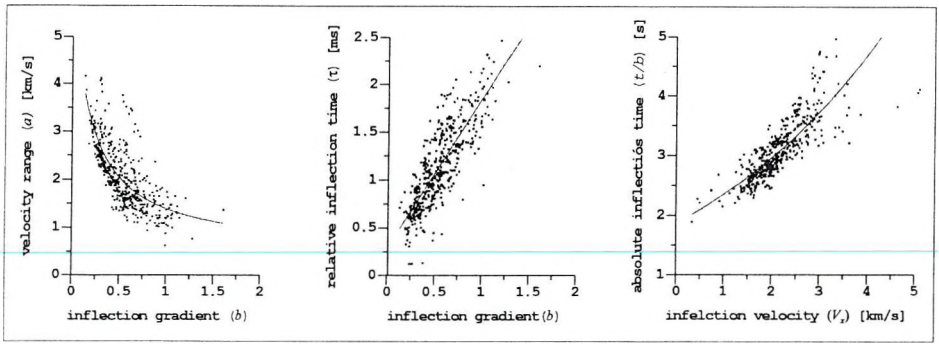

Fig. 5. Regression dependence of parameters related to the approximation function of the V_{rms} velocity functions

5. ábra. V_{rms} sebességfüggvények approximációs függvényeinek paraméterei közötti regressziós kapcsolat

4. Application of parametric interpolation

4.1. Parametric mapping

The second computing step of the parametric interpolation of the 3-D velocity field is a horizontal 2-D interpolation of parameters of 1-D approximation functions fitted to vertically spreading numerical sequences of the original stacking velocity samples. Horizontal grids of substantial or derived approximation function parameters could be imaged by isoline maps (*Fig. 6*) and these maps are useful 'sideproducts' of the parametric interpolation procedure.

The parameters of the analytical function used here to approximate the vertical variation in the velocity field can be interpreted in various physical ways and may be related to specific geological attributes of the test area. The density of stacking velocity function samples on the test area does not allow detailed geological analysis but significant regional phenomena could be detected on the parameter maps.

Deviation of the general- (*Fig. 7*) or near-surface vertical velocity gradient from values typical of normal compaction trends is mainly influenced by the grain size and mineral content of the sediments [MÉSZÁROS, ZILAHI-SEBESS 2001].

The inflection velocity (*Fig. 8*) pertaining to the point of the greatest increase may be related to the depth interval where — in the compaction

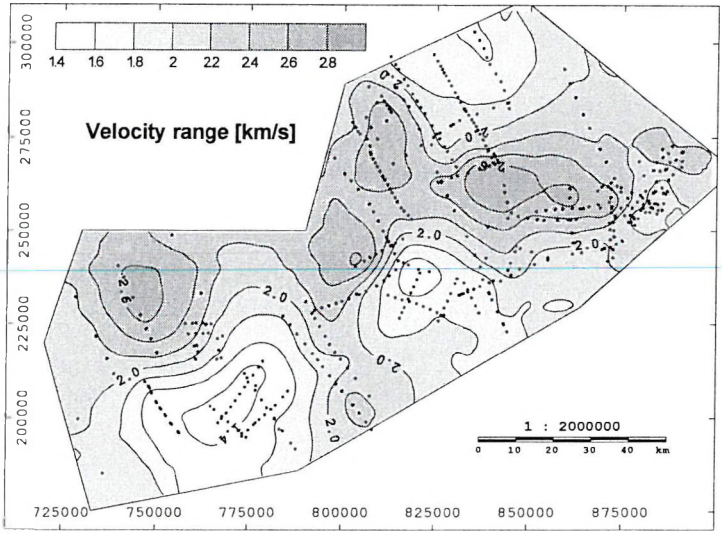

Fig. 6. Parameter map of the 'velocity range' on the test area
6. ábra. 'Sebesség sáv' paramétertérkép a teszterületen

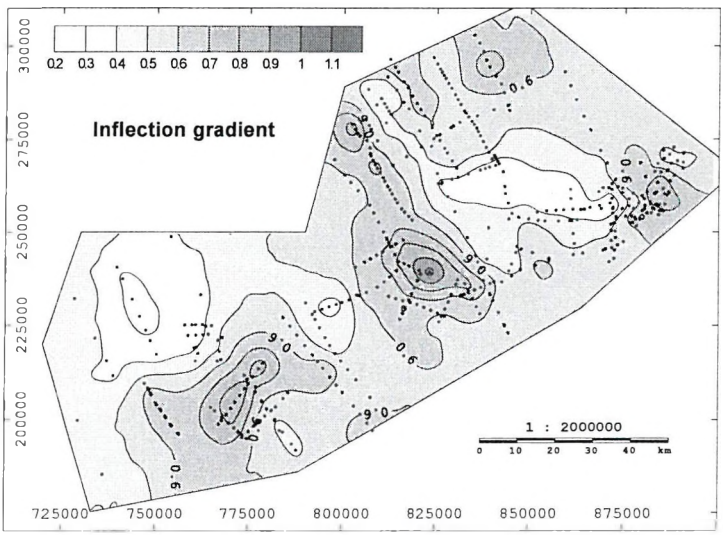

Fig. 7. Parameter map of the 'inflection gradient' on the test area
7. ábra. 'Inflexiós gradiens' paramétertérkép a teszterületen

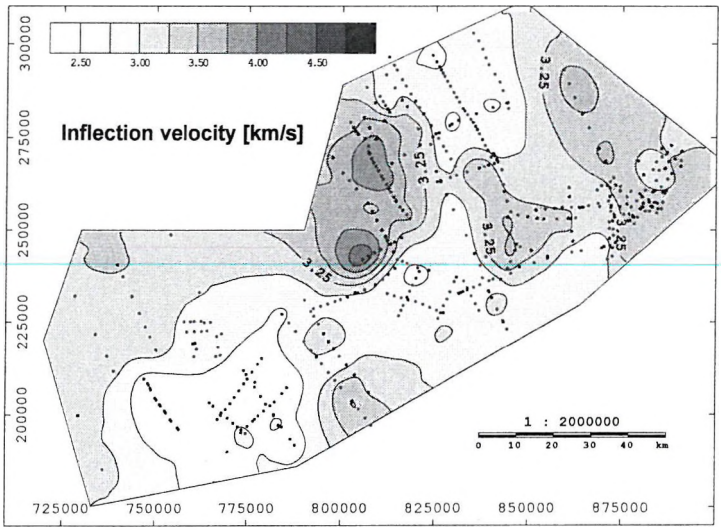

Fig. 8. Parameter map of the 'inflection velocity' on the test area
8. ábra. 'Inflexiós sebesség' paramétertérkép a teszterületen

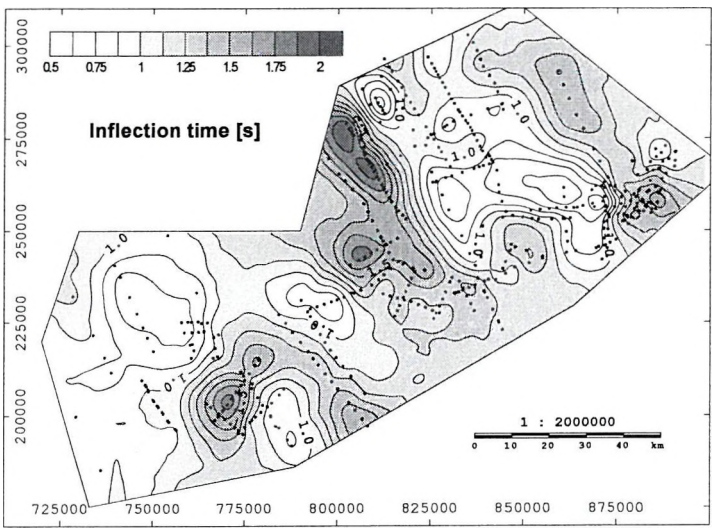

Fig. 9. Parameter map of the 'inflection time' on the test area
9. ábra. 'Inflexiós idő' paramétertérkép a teszterületen

lithostatic effect and age of the rock predominate, correlating well with depth [MESKÓ 1994], but the lithogenesis is by no means perfect. Among other aspects, these quality features could be related to the isoline map (see *Fig. 9)* of the derived parameter τ/b (inflection time).

One of the reasons for negative inflection time anomalies may be the uplifting movement periods in the prehistory of the basin evolution that took place locally by basement geometry as was detected using other, larger scale, indicators in some areas of the Pannonian basin. This type of supposed tectonic mechanism is also supported by computer modelling [HORVÁTH, CLOETHING 1996].

4.2. Depth conversion

In the case of parametric interpolation, the entire interpolated 3-D seismic velocity field of an area to be studied is represented by horizontally gridded numeric parameters of the 1-D analytical function (defined by parameters varying in the horizontal plain) which is used to approximate the field variation in the vertical direction.

One of the typical practical applications of such datasets is a conversion to depth of seismic reflection horizons resulting from conventional seismic interpretation, initially given vertically in reflection time and irregularly sampled in the horizontal direction. The above- mentioned type of application is demonstrated by the isoline depth map (*Fig. 11*) converted from the reflection time map (*Fig. 10*) compiled using seismic interpretation data of the Pre-Pannonian basement horizon in the test area (approx. 1500 km of overall section length).

Conversion of reflection time values into depth at specific places of the horizontal plane needs (as usual) the reflection time-based interval velocity function calculated by using the approximation parameters of the V_{rms} field existing at the given point, especially according to eq. (7) in the case of the approximation function introduced in *Section 2.2.*

Numeric integration (according to eq. (8)) of datasets with required accuracy of the given task, gained by sampling along (vertical) reflection times of the interval velocity function, calculated from 0 time (surface) to the reflection time to be converted, provides a corresponding two-way depth divided by the constant time sampling amount of the interval velocity function.

For a reliable assessment of the whole application, an isoline map of percentage differences has been compiled on the test area between two Pre-Pannonian depth surfaces obtained strictly by seismic interpretation followed by parametric interpolation-supported depth calculation and by well-stratigraphy correlation.

A selection from the well-stratigraphic database of the Hungarian Office for Mining and Geology with wells on the test area reaching a Pre-Pannonian basement, that were used as a source for compiling the depth map of the basement, is loaded with inconsistencies. The real checking was limited to a consistent subset of the database selection including just 250 items, the inhomogeneous location distribution of which slightly degrades the quality of the assessment.

Even though there are drawbacks of the dataset, the depth differences between the basement surfaces gained from seismic interpretation and well-stratigraphy are less than 10% for most of the area except locations of several small concentrated anomalies (*Fig. 12*).

In practice, such depth differences are usually eliminated by correction feedback including seismic interpretation itself. Excluding that particular way of correction especially in this case makes the reliability assessment of the parametric interpolation independent of the effects of other methods. Assessment of the average error level in the current application of parametric interpolation (which probably differs from the values of other areas) depends on the aim of the actual usage of the data.

5. Conclusions

Interpolation of seismic velocity fields is an indispensable part of structural geological investigations that use seismic interpretation data (*Section 1*). An alternative method for the same objective is the parametric interpolation introduced here (*Section 2.1*), which has two specific benefits compared with other methods:

— It simplifies the calculation task originally rising in most cases as a 3D problem to a 1-D approximation and a 2-D interpolation executed sequentially. Consequently it could be performed by relatively simpler software tools.

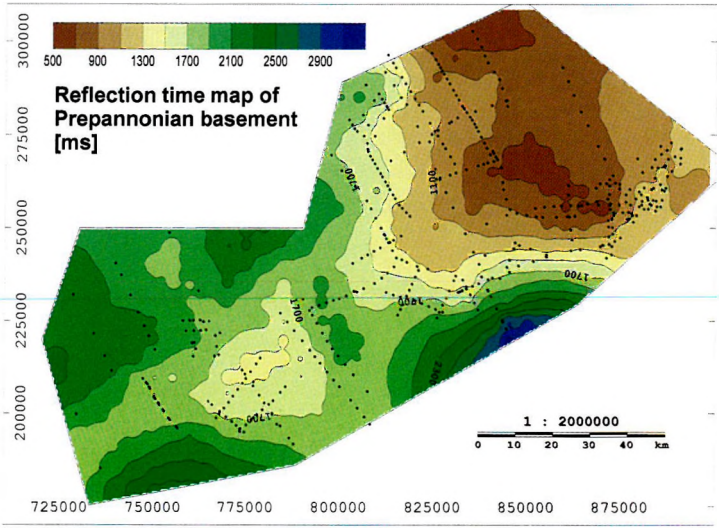

Fig. 10. Reflection time map of the Pre-Pannonian basement compiled from seismic interpretation data of the test area (apx. 1500 km of overall section length)
10. ábra. A pre-pannon aljzat szeizmikus értelmezési adatokból (kb. 1500 km össz szelvényhossz) kapott reflexiós időtérképe a teszterületen

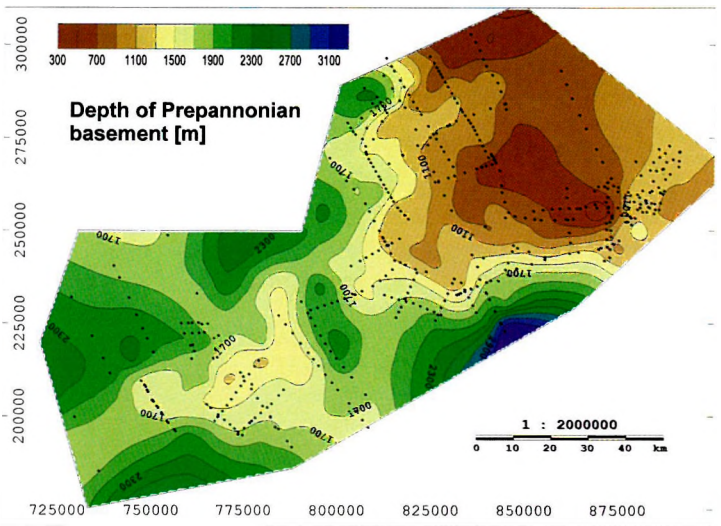

Fig. 11. Map of the Pre-Pannonian basement depth calculated using the velocity field defined by parametric interpolation
11. ábra. A pre-pannon aljzat mélységtérképe parametrikus interpolációval megadott sebességtér felhasználásával számolva

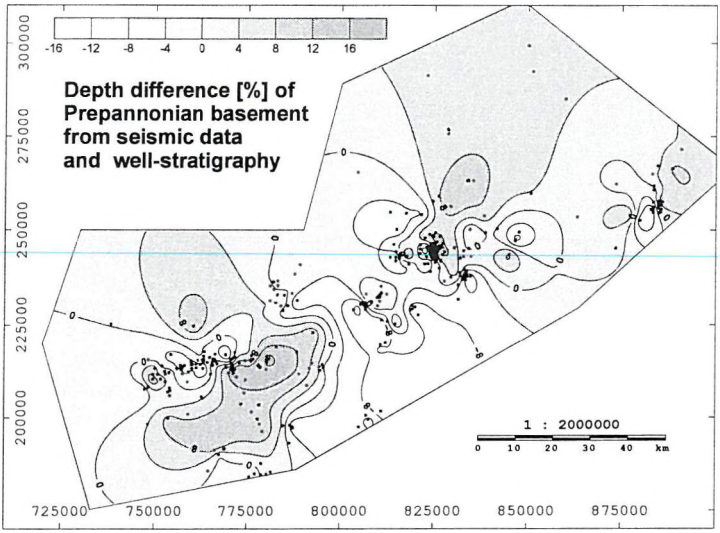

Fig. 12. Distribution map of the depth difference percentage in the test area calculated between Pre-Pannonian basement depths maps compiled from seismic interpretation and well-stratigraphy data

12. ábra. Fúrási rétegsorokból és a szeizmikus értelmezésből szerkesztett pre-Pannon mélységtérképből származó százalékos mélységek különbségeinek térképe a teszterületen

— It is possible to transfer the slowly changing anisotropy of the input velocity field to the interpolated result without special mathematical modules addressed to this particular purpose.

It is shown (*Section 2.3*) that the fitting of approximation functions selected for parametric interpolation purposes is possible with such a low level of error as 5–50 m/s, which is within the range of accuracy of the original numeric datasets. This is supported by real datasets of more than one thousand NMO velocity functions from the Pannonian Basin.

Regression analysis of parameter sets obtained by optimized fitting of selected approximation functions to NMO velocity functions on the test area shows an interdependence between them (*Section 3*). Clarification of the revealed dependence is planned for a future investigation.

Parameter maps are seamlessly compilable during the process of parametric interpolation. These are capable of exploring regional characteristics of the investigated area obtainable with perhaps less effort than for other types of methods (*Section 4.1*).

Transformation from seismic reflection time to depth based on a parametrically interpolated seismic velocity field which was initially described by 486 distinct numeric velocity functions provided a result with an accuracy adequate for practical requirements.

The computing principle of parametric interpolation demonstrated above is of a general nature and it is not necessary to restrict for the application to interpolating 3-D seismic velocity fields. The chance of successful applications always arises when interpolation of such a kind of multidimensional (even abstract) field is needed, in case of which a section of the field itself along one of the coordinate axes could easily be approximated by a suitably chosen 1-D analytical function defined by parameters dependent on the location in the subspace of the given section.

Acknowledgements

The author wishes to thank MOL (the Hungarian Oil and Gas Co.), the Information Centre of the former Hungarian Geological Survey, and the Eötvös Loránd Geophysical Institute for permission to use national data for the purpose of this project. The author is grateful to all colleagues for practical contributions in the form of data gathering and selection. Ernő Prácser deserves special thanks not only for making his own software available but also for operating it to obtain approximation results. Dorothy Szabó `s painstaking work is highly appreciated.

REFERENCES

HORVÁTH F., CLOETINGH S. 1996: Stress-induced late-stage subsidence anomalies in the Pannonian basin. Tectonophysics, **266**, pp. 287–300

MESKÓ A. 1977: Seismics I. Eötvös L. University, Faculty of Natural Sciences, Budapest (in Hungarian) 382 p.

MESKÓ A. 1994: Elastic Waves in Earth (in Hungarian). Akadémiai Kiadó, Budapest pp. 118–139

MÉSZÁROS F., ZILAHI-SEBESS L. 2001: Compaction of sediments with great thickness in the Pannonian Basin. Geophysical Transactions, **44**, 1, pp. 21–48

SHARMA S. P., PRÁCSER E., ROY K. K. 2005: Joint Inversion of Seismic Refraction and Magnetotelluric Data for Resolving Deeper Subsurface Structure. Acta Geod. Geoph. Hung., **40**, 2, pp. 241–258

VEEKEN P., FILBRANDT J., AL RAWAHY M. 2005: Regional time-depth conversion of the Natih E horizon in Northern Oman using seismic stacking velocities First Break **23**, August 2005

Szeizmikus sebességtér parametrikus interpolációja

DETZKY Gergely

A reflexiós szeizmikus kutatásban a szerkezetföldtani értelmezést hagyományosan reflexiós, idődimenzióban megjelenített szelvényeken végzik. Ahhoz, hogy a reflexiós idődimenzióban végrehajtott műveletek által eredményezett szerkezetföldtani információk felhasználhatók legyenek más egyéb forrásból származó részletező szerkezetföldtani adatokkal, szükség van megfelelő, kétirányú transzformációs eljárásra a reflexiós idő- és mélységtér dimenzió között. Ez a művelet elválaszthatatlan része a reflexiós szeizmikus értelmezést is magába foglaló alkalmazott földtudományi projekteknek. Sok hagyományos számítási módszer létezik ennek a feladatnak a megoldására. Ezek legtöbbje valamilyen direkt interpolációs eljárást alkalmaz a 3D sebességmező térben szabálytalan eloszlású mintavételi értékeire. Jelen írás egy újszerű numerikus módszert javasol ugyanerre a célra, a parametrikus interpolációt. Ez az eredetileg 3D-ben felálló probléma megoldását egy 1D közelítésre és egy azt követő 2D interpolációra egyszerűsíti, mely lehetőséget ad a feladat jóval könnyebben kezelhető szoftveres eszközökkel történő megoldására. Az eljárás elvéből következően, a számítás a ritkán mintavételezett területek esetén is stabilan megbízható marad. A javasolt eljárás további előnye az üledékes medencék sebességmezőinek gradiens viszonyaira jellemző anizotrópia eredendő leképezése, külön ezt a célt megoldó speciális numerikus eszköz nélkül.

ABOUT THE AUTHOR

Greg Detzky (1957) graduated as a geophysical engineer from Moscow Geological Prospecting Institute in 1981, and since that time he has been working for the Eötvös Loránd Geophysical Institute. He was awarded a second diploma (economic engineering in the mining industry), by Miskolc University, in 1986. In the 1980s, he was mainly concerned with field seismic work. Between 1995 and 2000 he established the bases of the National Seismic Database at ELGI. He then moved to his present post in the Department of Geoinformatics, where he is currently primarily concerned with geophysical database management activities. Two recent projects — supported by the EU — involved him in helping to establish an internet-based international geophysical data service. He is author or co-author of many publications and conference presentations.